An ESCRT-dependent pathway coordinates Nuclear and Cytoplasmic Spatial Protein Quality Control at Nuclear Vacuolar Junctions

Emily M. Sontag [1,*,†,£], Fabián Morales-Polanco [1,£], Jian-Hua Chen[2], Gerry McDermott[2], Patrick T. Dolan[1,‡], Dan Gestaut[1], Mark A. Le Gros[2,3], Carolyn Larabell[2,3] and Judith Frydman[1,*]

[1] Department of Biology, Stanford University, Stanford, CA 94305, USA

[2] Department of Anatomy, School of Medicine, University of California San Francisco, San Francisco, CA 94158, USA

[3] Molecular Biophysics and Integrated Bioimaging Division, Lawrence Berkeley National Laboratory, Berkeley, CA 94720, USA

[*] Correspondence to: emily.sontag@marquette.edu; jfrydman@stanford.edu,

£ These authors contributed equally

† Current address: Department of Biological Sciences, Marquette University, Milwaukee, WI 53233, USA

‡ Current address: Quantitative Virology and Evolution Unit, National Institute of Allergy and Infectious Diseases, Bethesda, MD 20892, USA

Abstract.

Effective Protein Quality Control (PQC), essential for cellular health, relies on spatial sequestration of misfolded proteins into defined inclusions. Here we elucidate the coordination of nuclear and cytoplasmic spatial PQC. While cytoplasmic misfolded proteins concentrate in a cytoplasmic, perinuclear Juxta Nuclear Quality control compartment (JUNQ), nuclear misfolded proteins sequester into a perinucleolar IntraNuclear Quality control compartment (INQ). Particle tracking reveals the INQ and JUNQ converge to face each other across the nuclear envelope at a site proximal to the Nuclear-Vacuolar Junction (NVJ) marked by perinuclear ESCRT-II/-III protein Chm7. Strikingly, this ESCRT-dependent convergence facilitates VPS4-dependent vacuolar clearance of misfolded cytoplasmic and nuclear proteins, the latter entailing extrusion of nuclear INQ into the vacuole. We propose perinuclear ESCRT coordinates spatial PQC at nuclear-vacuolar contacts to facilitate vacuolar clearance of nuclear and cytoplasmic misfolded proteins.

Introduction

Misfolded proteins can acquire toxic conformations that disrupt essential cellular processes [1-6] leading to human diseases ranging from neurodegeneration to cancer [7-10]. Accordingly, cellular protein homeostasis (proteostasis) is maintained by a network of chaperones and clearance factors that promote protein quality control (PQC) [11-15]. One fundamental PQC strategy is to spatially sequester misfolded proteins into distinctly localized membrane-less compartments, likely to remove damaging conformers from the cellular milieu and concentrate them for more efficient refolding or clearance through either the ubiquitin-proteasome system (UPS) or endo-lysosomal pathways [11, 16-18]. Misfolded cytoplasmic proteins partition into distinct inclusions depending on their aggregation state. Insoluble amyloid proteins are sequestered into the Insoluble Protein Deposit (herein the IPOD) [4, 11, 19]. Soluble misfolded proteins are sequestered into small, dynamic, ER-associated structures called Q-bodies [17] which, during sustained stress, coalesce along the endomembrane system [20] into a Juxtanuclear Quality Control compartment (herein the JUNQ). Spatial PQC through the IPOD and JUNQ pathways is evolutionarily conserved and is present in yeast, worms and mammalian cells [11, 19]. Spatial PQC is also observed in the nucleus, as nuclear misfolded proteins are sequestered in a membrane-less intranuclear quality control compartment (herein the INQ), proximal to the nucleolus [18, 21, 22].

The relationship and overall coordination between spatial PQC of cytoplasmic and nuclear proteins is not well understood. Many studies showed cytoplasmic misfolded proteins being concentrated into the cytoplasmic JUNQ and cleared through an ER-anchored cytoplasmic UPS pathway [11, 19, 23, 24]. It has also been proposed that clearance of cytoplasmic misfolded proteins requires import into the nucleus, whereby the JUNQ would form an inclusion identical to the INQ [18].

54 Given the importance of protein quality control for cell survival and its relevance to understand
55 misfolding diseases, we here examined the logic and coordination of spatial PQC for nuclear and
56 cytoplasmic misfolded proteins. We unequivocally demonstrate the cytoplasmic localization of the
57 JUNQ and nuclear localization of the INQ. We further show the JUNQ and INQ home to opposite
58 sides of the nuclear envelope, at a site proximal to NVJ, which facilitates the extrusion of the INQ
59 for clearance into the vacuole in an ESCRT- and VPS4-dependent manner. Our study uncovers a
60 surprising degree of spatial coordination between nuclear and cytoplasmic PQC inclusions
61 providing an avenue for vacuolar clearance of misfolded proteins.

62

63 **RESULTS**

64 **Organelle-specific PQC compartments sequester nuclear and cytoplasmic misfolded**
65 **proteins**

66 To define the relationship and interplay between nuclear and cytoplasmic spatial PQC (Fig. 1a),
67 we utilized two validated models of protein misfolding: a temperature-sensitive variant of Firefly
68 Luciferase (herein LuciTs) that misfolds at 37 °C, and the Von Hippel-Lindau (VHL) tumor
69 suppressor, which is constitutively unfolded in yeast cells [25, 26]. We restricted their subcellular
70 localization to either nucleus or cytoplasm by inclusion of a Nuclear Localization Signal (NLS) or
71 a Nuclear Export Signal (NES), respectively. The expression of these PQC substrates was first
72 selectively induced by growth in galactose at the permissive temperature, and then repressed by
73 glucose exchange, which allowed measuring the kinetics of their clearance or spatial PQC (Fig.
74 1b). As previously described, both NLS- and NES-LuciTs and NLS- and NES-VHL are degraded

upon misfolding and are stabilized by proteasomal inhibition with either MG132 or Bortezomib [27] (Extended Data Fig. 1a and Ref [27]).

To initiate LuciTs misfolding and monitor the fate of the misfolded species, the cells were shifted to 37 °C and evaluated using time-resolved fluorescence microscopy (Fig. 1b). Under folding-permissive conditions, NLS- and NES-GFP-LuciTs were diffusely localized in the nucleus or cytoplasm, respectively (Time 0, Fig 1 c, d), but following the shift to 37 °C, both nuclear (NLS) and cytoplasmic (NES) LuciTs were rapidly concentrated into dynamic puncta in their respective cellular locations (Fig. 1c, d, and Supplemental video 1).

Over the course of the experiment, nuclear NLS-LuciTs coalesced into one intranuclear INQ inclusion (Time 30 min, Fig. 1c). In contrast, cytoplasmic NES-LuciTs puncta coalesced into two cytoplasmic inclusions, corresponding to the JUNQ and IPOD (Time 30 min, Fig. 1d), as previously observed for Ubc9Ts and VHL [11]. Of note, the NLS- and NES- LuciTs variants formed inclusions in both the absence or presence of proteasome inhibitor MG132 (Figure 1c, d), indicating that spatial sequestration into PQC compartments is not a consequence of proteasomal inhibition.

We used structured illumination (SIM) super-resolution microscopy to better define the nuclear and cytoplasmic location and morphology of PQC inclusions. Cells expressing LuciTs variants were incubated for 2 hrs at 37 °C, while cells expressing VHL variants were grown and fixed at both 30 and 37 °C. The nuclear envelope was visualized by immunostaining of nuclear pore protein Nsp1 (Nups, yellow) and DNA was visualized using Hoechst (blue) (Fig. 1e-h). The INQ, formed by nuclear misfolded protein, localized inside the nucleus in a pocket between the nuclear envelope (delineated by Nups) and the DNA (Fig. 1e and Supplemental video 2 for NLS-LuciTs at 37 °C, Fig. 1f for NLS-VHL at 30 °C Extended Data Fig. 1c for NLS-VHL at 37 °C). Line

98 intensity profile analyses confirmed the intranuclear localization of this INQ (Fig. 1e, f, Extended
99 Data Fig. 1c). Importantly, SIM and line intensity profile analyses unequivocally established that
100 the PQC inclusions formed by cytoplasmic misfolded proteins NES-LuciTs and NES-VHL reside
101 outside of the nucleus: one inclusion is adjacent to the nuclear envelope as expected for the JUNQ,
102 while the other inclusion is closer to the cell periphery as expected for the IPOD (Fig. 1g-h,
103 Supplemental video 2, Extended Data Fig. 1d). Similar results were obtained with NLS- and NES-
104 VHL at both 30 °C and 37 °C indicating PQC inclusion localization is not temperature-dependent
105 (Extended Data Fig. 1c-d). Consistent with their distinct localization, cytoplasmic and nuclear
106 misfolded variants also exhibit differential toxicity to cells; cytoplasmic misfolded proteins were
107 slightly more toxic, albeit less so than a polyglutamine expanded exon1 variant of Huntingtin
108 (herein mHTT) associated with Huntington's disease (Extended Data Fig. 1b). The increased NES-
109 LuciTs toxicity was only observed at 37 °C when it is misfolded.

110 We conclude that nuclear and cytoplasmic misfolded proteins are spatially sequestered in PQC
111 inclusions located in their cognate compartment, yielding the INQ and JUNQ respectively. These
112 results resonate with findings that UPS degrades nuclear and cytoplasmic misfolded proteins
113 through different chaperones and ubiquitination enzymes [27], indicating the nucleus and
114 cytoplasm have compartment specific PQC machineries.
115

116 **Proteasome inhibition disrupts nucleocytoplasmic transport**

117 Most commonly used PQC reporters (e.g., Ubc9Ts, VHL, Cpy*, and Luciferase, etc.), are smaller
118 than the 200 kDa nuclear permeability barrier [28-30]. To examine if passive diffusion across nuclear
119 pores could explain why some cytoplasmic misfolded proteins can form intranuclear inclusions,
120 we utilized a temperature-sensitive variant of Ubc9 (Ubc9Ts) [11, 17, 18]. Upon Ubc9Ts unfolding at

121 37 °C for 2 hours under conditions where the proteasome is active, SIM super-resolution
122 microscopy showed Ubc9Ts is sequestered solely in two cytoplasmic compartments – the
123 perinuclear JUNQ, clearly outside the nuclear pore boundary and the IPOD in the cell periphery
124 (Fig. 2a, Supplemental Video 3). Treatment at 37 °C with added proteasome inhibitor MG132,
125 increased the fraction of cells containing Ubc9Ts inclusions, but in addition to the two cytoplasmic
126 inclusions as above, some cells (around 13%) had an additional Ubc9Ts inclusion inside the
127 nucleus (Fig. 2b, Extended Data Fig. 2a, Supplemental Video 3). Similar results were obtained for
128 another PQC substrate, VHL (Extended Data Fig. 2b). Interestingly, line intensity profile analyses
129 of both Ubc9Ts and VHL showed that the nuclear INQ and cytoplasmic JUNQ inclusions formed
130 in close proximity but separated by nuclear pores (Fig. 2b), These results confirmed that, absent
131 an NLS or NES localization tag, cytoplasmic proteins that can passively diffuse into the nucleus,
132 primarily form cytoplasmic inclusions, but under conditions of proteasome inhibition can also
133 form an additional distinct nuclear INQ in a small fraction of cells.

134 To reconcile the finding that spatial sequestration into a nuclear or a cytoplasmic PQC inclusion
135 depends on a misfolded protein's subcellular location when they misfold (Fig. 1a) with the fact
136 that MG132 leads to a small fraction of cells having a nuclear Ubc9Ts and VHL inclusion, we
137 hypothesized that prolonged proteasome inhibition may alter nucleocytoplasmic trafficking and
138 decrease protein export from the nucleus. Indeed, toxic misfolded proteins, such as the
139 polyglutamine expanded mHTT, are shown to impair nucleocytoplasmic transport [31, 32].

140 We examined the effect of MG132 on nucleocytoplasmic transport using a previously
141 characterized NLS- and NES-tagged shuttling GFP (sGFP) that migrates between the nucleus and
142 cytoplasm [31, 33] (Fig. 2c, d). As a control, we observed toxic mHTT expression caused nuclear
143 retention of sGFP as described (Fig. 2c, d). Of note, proteasome inhibition with MG132 caused

144 sGFP nuclear retention to the same extent as mHTT (Fig. 2c, d). This experiment was performed
145 in leptomycin B-sensitive *crm*^{T539C} cells, which permitted the use of leptomycin B (LMB) as a
146 positive control for blocked nuclear export (Fig. 2c, d), but similar results were obtained using WT
147 BY4741 yeast cells (not shown). Our finding that proteasome inhibition impairs nuclear export to
148 an extent comparable to toxic mHTT may explain the increased retention of misfolded protein
149 Ubc9Ts in the nucleus. Future studies should examine the basis for reducing nuclear export when
150 proteostasis is impaired [31, 34, 35].

151 To directly assess if cytoplasmic misfolded protein clearance requires their import to the nucleus,
152 we examined Ubc9Ts clearance in cells carrying a temperature-sensitive mutation in nuclear pore
153 complex (NPC) protein Nup116 (*nup116-5)*. At 37 °C, the *nup116-5* mutation seals nuclear pores
154 over the cytoplasmic face of NPCs blocking any transport into and out of the nucleus [36] (Fig. 2f,
155 *i*). WT and *nup116-5* cells expressing Ubc9Ts were shifted to 37 °C for 1 hour prior to the glucose-
156 repression to ensure nuclear pores become completely sealed prior to measuring Ubc9Ts clearance
157 rates (Figure. 2e, *ii*). If degradation of misfolded Ubc9Ts requires import into the nucleus, it should
158 be abrogated in *nup116-5* cells at 37 °C. We did not observe any significant differences in the rate
159 and the extent of Ubc9Ts degradation in *nup116-5* cells, suggesting that transport into the nucleus
160 is not required for its clearance (Figure. 2f, *ii-iii*; Extended Data Fig. 2c).

161 We next examined whether nuclear proteasomes participate in clearance of a cytoplasmic
162 misfolded protein. To this end, we used *sts1-2* cells that carry a mutation in Sts1, a protein required
163 for import of proteasomes into the nucleus and facilitate the degradation of nuclear proteins. At 37
164 °C, nuclear localization of proteasomes is lost in *sts1-2* cells [37-40] (Fig. 2g panel *i*). However,
165 preventing nuclear localization of proteasomes had no effect on the clearance of misfolded
166 Ubc9Ts, consistent with cytoplasmic degradation (Fig. 2g, panel *ii-iii*; Extended Data Fig. 2d).

167 These experiments indicate that import of misfolded proteins and proteosomes into the nucleus is
168 dispensable to degrade misfolded Ubc9Ts.

169

170 **INQ and JUNQ home into adjoined locations on opposite sides of the nuclear envelope**

171 Given that nuclear and cytoplasmic Ubc9Ts inclusions in MG132-treated cells localized to
172 opposite sides of the nuclear envelope (Fig. 2b), we next sought to define the spatial relationship
173 between INQ and JUNQ in live cells. To this end, NLS- LuciTs and NES- LuciTs were co-
174 expressed in WT yeast cells at 25 °C for 6 hr before repressing their synthesis with glucose. Cells
175 were shifted to 37 °C to unfold both proteins simultaneously, and inclusion formation was
176 monitored in real-time by live cell time-lapse fluorescence microscopy and particle tracking
177 analysis (Fig. 3a, b; Extended Data Fig. 3a; Supplemental Videos 4, 5). Spatial sequestration of
178 the NLS- and NES- misfolded proteins into motile condensates occurred with similar kinetics
179 independently in the nucleus and the cytoplasm. Once formed, puncta moved dynamically toward
180 each other, with nuclear and cytoplasmic inclusions converging on a specific location proximal to
181 the nuclear envelope (Fig. 3a). Of note, even after homing to this location, the two inclusions
182 remain distinct and separated; however, they co-migrated around the nuclear periphery as if
183 tethered to each other across the nuclear envelope. Particle tracking analyses measuring the
184 location and distance of NLS- and NES-LuciTs inclusions in 2D space showed the nuclear and
185 cytoplasmic inclusions homed into adjoining locations between 10 and 20 minutes after shifting
186 to 37 °C, and then continued moving in a coordinated manner throughout the duration of the
187 imaging experiment (Fig. 3b; Extended Data Fig. 3a; Supplemental video 5). While the distance
188 between these two inclusions decreased rapidly during homing, once they came together they
189 maintained a largely stable short distance, suggestive of a tether, throughout their co-migration for

190 the remainder of the experiment. Similar results were obtained if the fluorescent markers in NLS-
191 and NES-LuciTs were reversed (not shown) as well as for NLS- and NES-VHL (Extended Data
192 Fig. 3b). These observations, supporting our findings with Ubc9Ts, suggest a novel mechanism
193 coordinating convergence of nuclear and cytoplasmic PQC compartments.

194 The spatial relationship between the INQ and the JUNQ was confirmed using SIM super-resolution
195 microscopy. Cells co-expressing NLS-LuciTs and NES-LuciTs were incubated at 37 °C for 2 hrs
196 and then fixed and immunostained to detect nuclear pores (Fig. 3c). SIM combined with line
197 intensity profile analysis confirmed the INQ and JUNQ adjoined each other on opposite sides of
198 the nuclear envelope, separated by the nuclear pores (Fig. 3c; Supplemental video 6).

199

200 **Nuclear pores play a role in INQ-JUNQ convergence at the nuclear periphery**

201 To understand the nature of the signal bringing together the INQ and JUNQ, we examined their
202 subcellular co-localization with specific nuclear and perinuclear structures. The INQ was near the
203 nucleolus but not in direct contact, suggesting the nucleolus is not driving this homing mechanism
204 (Extended Data Fig. 3c). We examined the relationship of the INQ-JUNQ homing signal with two
205 complexes that localize to a defined perinuclear location: the spindle pole body [41] (SPB) and the
206 LINC complex [42], both of which contain protein Mps3 spanning both layers of the nuclear envelope
207 (Extended Data Fig. 3d). Co-staining with Mps3 showed neither SPB nor LINC co-localize with
208 the INQ-JUNQ perinuclear site, suggesting they do not participate in the INQ-JUNQ homing
209 mechanism (Extended Data Fig. 3d).

210 To investigate the role of nuclear pores in INQ/JUNQ homing, we exploited the finding that
211 deletion of nuclear pore protein Nup120 causes nuclear pores to remain functional but become

212 clustered [43, 44]. We thus compared INQ and JUNQ formation and localization in WT and *nup120Δ*
213 cells. In *nup120Δ* cells, the JUNQ always forms next to the clustered nuclear pores (Fig. 3d, panel
214 *i*) while the INQ did not localize proximal to the nuclear pores, but instead was found anywhere
215 within the nucleus (Fig. 3d, panel *ii*). Surprisingly, if we co-expressed NLS- and NES-LuciTs in
216 *nup120Δ* cells, the INQ now homed to the clustered nuclear pores opposite the JUNQ (Fig. 3d,
217 panel *iii*). This finding suggests formation of the JUNQ at the cytoplasmic side of the nuclear pores
218 communicates a signal for INQ recruitment to this location (Fig. 3e).

219 We next asked if the intrinsically disordered phenylalanine-glycine (FG) repeats in the central
220 nuclear pore channel, which form hydrogels capable of amyloid-like interactions [45], facilitate INQ-
221 JUNQ homing. Using live-cell time-lapse microscopy we examined the localization of the INQ
222 and JUNQ in *nupΔFG* cells, carrying deletions in the FG repeat tracts of six nuclear pore proteins
223 that removes approximately 70% of the FG content from the nuclear pore [46]. We found that the
224 INQ and JUNQ still localized to the same perinuclear location in *nupΔFG* cells suggesting the
225 high percentage of FG-repeats are dispensable for homing (Extended Data Fig. 3e). Although, we
226 cannot exclude the possibility that that the remaining 30% of FG content is still sufficient to direct
227 convergence of the INQ and JUNQ to the proximity of nuclear pores.

228

229 **Cryo-soft X-ray tomography reveals the architecture of PQC inclusions in intact cells**

230 To examine the native cellular context of PQC compartments we used cryogenic Soft X-ray
231 Tomography (cryo-SXT). This synchrotron-based imaging approach can visualize and quantify
232 the ultrastructure of intact, unstained, cryo-preserved cells (Fig. 4a, Extended Data Fig. 4a, b) [47,
233 48]. cryo-SXT uses the characteristic linear absorption of X-rays by different subcellular organelles

234 to produce projection images of cellular ultrastructure to a few tens nanometers of spatial
235 resolution [49]. To derive the information content needed to study misfolded protein inclusions we
236 initially used cryo-SXT in correlation with cryo-fluorescence microscopy (Fig. 4b,i). The ability
237 to absorb X-rays varies with the type and density of biomolecules present in different
238 compartments, yielding characteristic linear absorption coefficients (LAC) (Fig. 4b, ii) [50-52]. Since
239 chaperone Hsp104 localizes to both the JUNQ and IPOD upon heat shock, while aggregation-
240 prone mHTT only localizes to the IPOD [11, 20], we visualized these PQC compartments by
241 expressing mHTT-ChFP in cells with chromosomally tagged HSP104-GFP [53]. The inclusions
242 were formed by 1 hr incubation at 37 °C and cells were flash frozen in capillary tubes and directly
243 imaged using cryo-SXT correlated with cryo-fluorescence microscopy (Fig. 4b, i). The LAC
244 values were used to identify the exact location of specific compartments and organelles in X-ray
245 tomograms of intact frozen yeast cells (Fig. 4b, ii), yielding a 3D reconstruction of the PQC
246 inclusions in the context of cellular architecture (Fig. 4c, Supplemental Video 7). Cryo-
247 fluorescence identified the PQC compartments, with Hsp104-only marking the JUNQ and co-
248 localized Hsp104 and mHTT marking the IPOD. This analysis revealed that protein inclusions
249 have a characteristic LAC that can be used to examine their location and size without the need of
250 fluorescence microscopy. Of note, this correlated fluorescence-cryo-SXT analyses confirmed both
251 the JUNQ and the IPOD are cytoplasmic, as previously described (Fig. 4c, Supplemental Video 7
252 and [11]).

253 We next used cryo-SXT to directly detect inclusions formed by NLS- and NES-LuciTs at 37 °C
254 through their characteristic LAC values. NES-LuciTs formed small, cytoplasmic, punctate Q-
255 bodies that could be seen congregating at a cytoplasmic, juxtanuclear location to form the JUNQ
256 (Fig. 4d, Supplemental Video 8). Thus, cryo-SXT indicates the JUNQ is not the homogeneous

257 large compartment suggested by diffraction-limited fluorescence imaging, but rather consists of
258 multiple dense "cores" that resemble Q-bodies. This conclusion, also supported by the irregular
259 JUNQ morphology in SIM and cryo-EM imaging (Fig. 1, Fig 5 and [54]), suggests the JUNQ is in
260 fact a collection of Q-bodies that congregate at a perinuclear location proximal to the nuclear
261 envelope (Fig. 4d, inset *ii*; Supplemental video 8).

262 Cryo-SXT analysis also revealed a link between cytoplasmic PQC and mitochondria. Individual
263 Q-bodies can associate with the surface of mitochondria (Fig. 4e) and the JUNQ and IPOD appear
264 surrounded by a mitochondrial cage (Fig. 4d, *i*). Confocal fluorescence microscopy of cells
265 expressing mito-GFP supported the mitochondrial association with Q-bodies (Extended Data Fig.
266 4d). However, PQC compartments still formed in cells with disruptions in mitochondrial fission
267 or fusion (Extended Data Fig. 4e) indicating mitochondrial structure does not direct PQC
268 compartment formation. Since previous studies placed Q-bodies on the ER membrane [17, 20], which
269 cannot be visualized by cryo-SXT, it is possible that Q-bodies are proximal to ER-mitochondrial
270 contact sites. Alternatively, the proximity to mitochondria may serve to place energy-intensive
271 PQC compartments in areas of the cell enriched in ATP production [55].

272 Cryo-SXT also confirmed that the intranuclear INQ is distinct from but resides near the nucleolus
273 (Fig. 4g). This conclusion is supported by confocal fluorescence microscopy with nucleolar protein
274 Nsr1 (Extended Data Fig. 3c, 4c and [18, 31]). The proximity of the nucleolus to the INQ is consistent
275 with the nucleolus' role in nuclear folding and assembly [21, 56-58] and suggest a possible link to the
276 INQ's function in nuclear PQC [56, 59].

277 Strikingly, our cryo-SXT imaging revealed an unexpected link of both INQ and JUNQ with the
278 vacuole. The entire JUNQ site was surrounded by nuclear-vacuolar inter-organelle contact sites
279 (Figure. 4f, red arrows; Supplemental Video 8). Remarkably, Q-bodies within the JUNQ area were

280 nestled within invaginations in the vacuolar membrane, suggestive of direct vacuolar engulfment
281 and raising the idea that the vacuole promotes JUNQ clearance (Figure. 4f, blue arrows;
282 Supplemental Video 8). The INQ was also proximal to the vacuolar side of the nucleus, indicating
283 both INQ and JUNQ are steered to the vicinity of nuclear-vacuolar contact sites (Fig. 4g). The
284 nucleus-vacuole contact sites are formed by a tethering Nuclear-Vacuolar Junction (NVJ) complex
285 between nuclear Nvj1 and vacuolar Vac8 (Fig. 4h and [60]). Consistent with the idea that the INQ
286 and JUNQ converge to the vicinity of NVJs, all nuclear pores in *nup120*Δ cells cluster at the
287 vacuole-contacting side of the nucleus [44].

288

289 **Nuclear-Vacuolar Junctions facilitate clearance of JUNQ and INQ**

290 The role of NVJs remains poorly understood, but it has been implicated in lipid droplet biogenesis,
291 nuclear envelope autophagy, amino acid metabolism and a specialized form of autophagy called
292 Piecemeal Microautophagy of the Nucleus (PMN), where portions of the nucleus invaginate into
293 the vacuole [61-66]. We assessed the co-localization of the JUNQ and the NVJ by expressing NES-
294 LuciTs or Ubc9Ts in cells carrying a chromosomally tagged Nvj1-GFP [53]. Live-cell time-lapse
295 microscopy revealed transient and dynamic interactions between JUNQ and Nvj1, whereby both
296 puncta came in contact and then separated (Fig. 5a; Extended Data Fig. 5a; e.g. observe 9 min to
297 11 min in Supplemental Video 9).

298 The architecture of perinuclear spatial PQC and the close association of the INQ and JUNQ in
299 relation to the NVJ were next examined using SIM super-resolution microscopy (Fig. 5b-e;
300 Supplemental Videos 10, 11). The NVJ, visualized via Nvj1 imaging, forms a basket-shaped
301 structure contouring the Nuclear Envelope and connected to the vacuole (Fig. 5d). In these super-
302 resolution images, the JUNQ, visualized by NES-LuciTs, was proximal to the cytoplasmic side of

303 the NVJ as observed by Cryo-SXT (Fig. 5b). Of note, the Q-body "assembly" substructure of the
304 JUNQ was evident in these images. On the other hand, the nuclear INQ, visualized by NLS-
305 LuciTs, was nestled between the concave nuclear side of the NVJ and the nuclear DNA (Fig. 5c).
306 Strikingly, we were able to observe in some cells the INQ being extruded through the NVJ to enter
307 the vacuole (Fig. 5e; Supplemental Video 12). These experiments suggest dynamic tethering of
308 the INQ and JUNQ to the NVJ vicinity account for the homing of these inclusions as well as the
309 slight fluctuations in distance between these inclusions observed in particle tracking experiments
310 in Fig. 3.

311 We next tested if NVJs play a role in INQ and JUNQ clearance using *nvj1Δ* or *vac8Δ* yeast cells.
312 Live-cell time course analyses provided an unexpected insight into NVJ function. In *nvj1Δ* cells,
313 nuclear and diffuse NLS-LuciTs formed an initial nuclear inclusion, but during the time-course,
314 some cells showed the INQ being egressed from the nucleus into the cytoplasm (Fig. 5f).
315 Strikingly, some of the egressed NLS-LuciTs puncta ended up co-localizing with NES-LuciTs
316 (Fig. 5f, inset; Supplemental Video 13; white arrowheads). Similar results were obtained when
317 cycloheximide was added together to the temperature shift (Extended Data Fig. 5b) to ensure all
318 the NLS-LuciTs is in the nucleus. We observed NLS-LuciTs extruded from the nucleus in the
319 *njv1*Δ but not the WT cells, confirming NVJ disruption leads to nuclear extrusion of the INQ.
320 Confocal microscopy in *nvj1Δ* and *vac8Δ* cells confirmed that NVJ disruption led to extrusion of
321 nuclear NLS-LuciTs into the cytosol, where it ended up co-localizing with NES-LuciTs puncta
322 (Fig. 5g; white arrowheads). Of note, deleting the NJVs does not disrupt INQ and JUNQ
323 convergence, as the INQ and JUNQ are still juxtaposed in both *nvj1Δ* and *vac8Δ* cells (Fig. 5g).

324 We next examined if deletion of the NVJ affects clearance of PQC inclusions. Indeed, we observed
325 dramatic increases in the fraction of cells containing NLS and NES-LuciTs inclusions in

326 *nvj1Δ* and *vac8Δ* cells compared to WT cells (Fig. 5h, panels *i, ii*; Extended Data Fig. 5c,d), as
327 well as the levels of misfolded protein (Extended Data Fig. 5e). MG132 addition led to a
328 synergistic enhancement in the number of cells with NES-LuciTs inclusions, suggesting the NVJ
329 and the proteasome represent distinct cytoplasmic clearance pathways (Extended Data Fig. 5c).
330 The synergy effect for NLS-LuciTs inclusions was marginal, perhaps because the higher fraction
331 of cells with INQs poses a ceiling effect to our measurements. Alternatively, the NVJ may play a
332 greater role in the clearance of nuclear protein inclusions (Extended Data Fig. 5b). Further
333 supporting a role in misfolded protein clearance, NVJ deletion sensitizes cells to proteotoxic stress
334 (Fig. 5i). Both *nvj1Δ* and *vac8Δ* cells are sensitive to treatment with proline analog AZC, which
335 induces widespread misfolding of newly translated proteins (Fig. 5i).

336 The findings that the INQ and JUNQ converge on nuclear-vacuolar contact sites and that the NVJ
337 is required for efficient clearance of nuclear and cytoplasmic inclusions define nuclear-vacuolar
338 contacts as cellular hubs for spatial protein quality control.

339

340 **ESCRT proteins are required for INQ-JUNQ homing and clearance at the vicinity of NVJs**

341 The relationship observed between spatial PQC and the nuclear-vacuolar contact sites led us to
342 examine the role of the perinuclear ESCRT-II/III protein Chm7 (CHMP7 in mammals) which
343 participates in nuclear envelope sealing and nuclear pore quality control [67-69] (Fig. 6a, *i*).

344 In yeast, Chm7 normally looks diffuse throughout the cytoplasm (Extended Data Fig. 6a) and
345 becomes associated with a unique site in the nuclear envelope upon activation. The active
346 conformation of Chm7 can be induced by deleting auto-inhibitory helices in the ESCRT-III
347 domain [herein $Chm7_{OPEN}$] [69, 70]. Strikingly, activated $Chm7_{OPEN}$ localized to a single site in the

348 nuclear envelope in close proximity with both INQ and JUNQ (Fig. 6a, *ii*), suggesting that this
349 perinuclear ESCRT protein marks the site of INQ and JUNQ convergence for vacuolar delivery.

350 We next examined whether loss of Chm7 impacts INQ and JUNQ subcellular localization. In
351 *chm7Δ* yeast cells, both INQ and JUNQ still formed and migrated to the perinuclear region, but
352 they no longer converged to the same location (Fig. 6b. These results reveal a novel role for the
353 Chm7 ESCRT protein as recruiting nuclear and cytoplasmic PQC compartments to a specific
354 location on the nuclear envelope, either for further clearance or terminal sequestration.

355 Since Chm7 is an ESCRT II/III protein, we next examined the role of other ESCRT proteins in
356 spatial PQC: the ESCRT-I Vps23 and the membrane bound phosphatidylinositol 3-kinase (PI3K)
357 complexVps34-Vps15. Vps23 is a component of the ESCRT-I complex that binds to ubiquitinated
358 cargo proteins and mediates their vacuolar transport [71-73]. The Vps34-Vps15 complex is essential
359 for protein sorting to the vacuole and has been shown to localize to nuclear pores at NVJs [74-77].

360 We co-expressed NLS- and NES-LuciTs in either WT, *vps23Δ*, *vps34Δ*, and *vps15Δ* cells, and
361 followed their fate by inducing unfolding at 37 °C. While INQ and JUNQ formed in both WT and
362 ESCRT mutants, the spatial relationship between INQ and JUNQ was disrupted in the ESCRT
363 deletions. All three ESCRT mutants showed similar aberrant localization phenotypes which
364 included cells in which the INQ and JUNQ were no longer homed as well as cells displaying
365 cytoplasmic egress of the INQ (Fig. 6c, Extended Data Fig. 6b). Strikingly, in a subset of *vps23Δ*
366 and *vps34Δ* cells we observed a possible intermediate for nuclear egress of the INQ, whereby the
367 NLS-LuciTs inclusion was fully enveloped by the nuclear membrane in what appears to be a
368 budding event (Fig. 6c, Extended Data Fig. 6b). These data suggest that the ESCRT pathway plays
369 a role in homing of INQ and JUNQ to the NVJ as well as extrusion of the INQ, likely to mediate

370 vacuolar delivery and clearance. Furthermore, when this process is perturbed, the INQ can
371 sometimes bud into the cytoplasm.

372 We next asked if this perinuclear ESCRT pathway promotes vacuolar clearance of the INQ and
373 JUNQ. Since vacuolar engulfment often requires the AAA-ATPase Vps4, which functions by
374 disassembling ESCRT-III complexes [78, 79] (Fig. 6d), we examined the effect of deleting Vps4 on
375 INQ and JUNQ clearance as described above. Indicating that Vps4 is required for clearance of
376 both INQ and JUNQ, *vps4*Δ cells contained more NLS- and NES-LuciTs inclusions than WT
377 controls (Fig. 6e). Strikingly, NLS-LuciTs also egressed into the cytoplasm in some *vps4*Δ cells
378 (Fig. 6f), supporting the notion Vps4 mediates INQ budding into the vacuole. Together, these
379 results indicate that nuclear misfolded proteins sequestered in the INQ are homed to the nuclear
380 side of NVJ to be extruded out of the nucleus and into the vacuole in an ESCRT family protein-
381 dependent manner.

382

383 **Vacuolar clearance of proteins in INQ and JUNQ**

384 To further examine vacuolar targeting of nuclear and cytoplasmic inclusions in yeast we utilized
385 the pH sensitive protein sensor Keima (Fig. 7a). Keima has a pH-sensitive excitation spectrum,
386 with a maximum of 440 nm at neutral pH and a maximum of 558 nm in acidic environments such
387 as the vacuole [80, 81], whereas its emission spectrum has a pH-insensitive maximum at 620 nm [80].
388 Since Keima in yeast has a weak emission intensity and is easily bleached [81], we used N-terminal
389 tagging with two consecutive Keima moieties to visualize NLS- and NES-LuciTs (herein
390 2xKeima-LuciTS; Fig. 7a, b, schematic). In the folded state, both NLS-LuciTS and NES-LuciTS
391 proteins were diffusely located in the nucleus and the cytoplasm respectively, with the excitation

392 wavelength characteristic of a neutral pH environment. Upon misfolding at 37 °C, both NLS-
393 LuciTs-Keima and NES-LuciTs-Keima formed the nuclear INQ and cytoplasmic JUNQ
394 respectively maintaining the neutral pH environment maximum emission after 404 nm excitation,
395 suggesting that inclusion formation takes place initially in their respective subcellular location.
396 However, continued incubation at 37 °C yielded regions of characteristic acidic environment
397 emission at 620 nm following 558 nm excitation appearing in a time-dependent manner for both
398 inclusions (Fig. 7c, d, Extended Data Fig. 7a, b). The kinetics of acidification of the JUNQ was
399 slower than for the INQ, consistent with its slower clearance kinetics (Extended Data Fig. 1a). For
400 the INQ, the red shift appears to initiate at the nuclear envelope boundary on what seems to be
401 almost full co-localization, with an elongated structure observed extending from the inclusion and
402 entering the vacuole on some cells (Fig. 7c). The slower degradation kinetics of the JUNQ coupled
403 with the low quantum yield and quick photobleaching of Keima precluded continuous live-
404 imaging of the JUNQ, but an imaging time course of different regions on the same slide showed
405 also areas of almost full colocalization and also multiple red only foci arising proximal to the
406 JUNQ (Fig. 7d; Extended Data Fig. 7a-b). Of note, these experiments were carried out under
407 conditions of ongoing proteasome degradation indicating that under these experimental conditions
408 vacuolar targeting seems to occur in parallel to UPS-mediated clearance of misfolded proteins.

409 The contribution of vacuolar and proteasomal pathways in the clearance of misfolded nuclear and
410 cytoplasmic proteins was independently assessed using immunoblot analyses (Fig. 7e-f). Briefly,
411 GFP-tagged NLS- and NES-LuciTs were expressed under permissive conditions, followed by
412 glucose repression, as described in Fig 1. Following unfolding, the levels of remaining luciferase
413 were examined after 2 and 4 hrs at 37 °C by immunoblot analyses probing for the GFP moiety.
414 The contribution of proteasomal clearance was assessed by addition of 50 μM Bortezomib [27, 82]

415 (Bz) at T=0, while the contribution of vacuolar clearance was assessed using cells deleted for Pep4,
416 required for maturation of vacuolar proteinases, supplemented with 1mM PMSF to inhibit vacuolar
417 serine proteases [83]. As expected, the levels of full length nuclear and cytoplasmic luciferase
418 decreased as a function of time, and were partially stabilized by proteasomal inhibition (Figure 7
419 e,f; Extended Data Fig. 7c-e). Inhibition of vacuolar proteases in the *pep4*Δ cells stabilized both
420 the nuclear and cytoplasmic full-length proteins [84, 85](Figure 7c-e; Extended Data Fig. 7c, e).
421 Interestingly, we also observed a range of GFP-positive degradation products in the WT and +Bz
422 cells that disappear when the vacuolar proteases were inhibited (Figure 7g), which is a hallmark
423 of vacuolar targeting of GFP-tagged proteins [64, 65, 83, 86-89]. Quantification of the intensity of
424 degradation fragments relative to initial full-length protein confirmed the reduction in clearance
425 when vacuolar proteases are inhibited (Fig. 7g). Moreover, a longer exposure reveals fewer bands
426 and a completely different banding pattern between WT and protease inhibited cells (Extended
427 Data Fig. 7c).

428 The finding that inhibiting vacuolar proteases stabilizes NLS-LuciTs supports the existence of a
429 pathway to transfer nuclear PQC substrates to the vacuole. To independently corroborate this, we
430 next carried out live-cell time resolved imaging of the dynamic clearance of the INQ through the
431 vacuole (Fig. 7g). The INQ was visualized via NLS-LuciTs-GFP and the vacuole using the styryl
432 dye FM4-64 commonly used to visualize endocytosis and vacuolar membrane dynamics [90] (Fig.
433 7g; Supplemental Video 14). Since GFP fluorescence is quenched by the acidic vacuolar
434 environment, NLS-LuciTS[84, 85, 91, 92] (Fig. 7g; supplemental video 14; Extended Data Fig. 7d). In
435 WT cells, the INQ is opposed to the vacuole at the start of the time course and appears to be pulled
436 into the vacuole as a function of time. Fascinatingly, when the nuclear-vacuolar contact is
437 disrupted in *nvj1*Δ, the INQ is unable to interact with and enter the vacuole and moves dynamically

438 without becoming degraded (Fig. 7g, second row; Supplemental Video 15). Strikingly, in the vast
439 majority of *vps4*Δ cells, the INQ looks still proximal to the vacuole but does not get cleared,
440 supporting a role for Vps4-mediated membrane scission for INQ vacuolar engulfment (Fig 7g,
441 third row; Supplemental Video 16).

442

443 **DISCUSSION**

444 Spatial sequestration of misfolded proteins into membrane-less inclusions is an integral step in
445 PQC. Here, provide insights into the logic of spatial PQC. We demonstrate that cytoplasmic
446 misfolded proteins are sequestered into a cytoplasmic perinuclear JUNQ compartment, while
447 nuclear misfolded proteins are sequestered into a nuclear peri-nucleolar INQ compartment (Figure
448 8a, b). Previous studies identified distinct nuclear and cytoplasmic PQC pathways that target
449 proteins that misfold in these compartments for ubiquitin-dependent proteasomal degradation in
450 the nucleus and cytoplasm respectively [27, 93] (Figure 8b). Supporting the concept that nuclear and
451 cytoplasmic proteins are cleared in the compartment where they misfold, these studies identified
452 distinct ubiquitin ligases and ubiquitin linkage requirements in the nucleus and cytoplasm that
453 promote PQC [27, 94]. We find spatial sequestration is also compartment specific, with nuclear and
454 cytoplasmic inclusions forming in the nucleus and cytoplasm independently. These distinct PQC
455 compartments converge to face each other across the nuclear envelope at a site proximal to the
456 Nuclear-Vacuolar Junctions (NVJ) (Figure 8c). The homing process seems to be coordinated by
457 nuclear pores and a perinuclear ESCRT pathway involving ESCRT II/III protein Chm7 (Figure
458 8c). We further propose that proteins sequestered in both JUNQ and INQ undergo Vps4-dependent
459 vacuolar degradation (Figure 8c, inset).

460

461 Cryo-SXT and super-resolution imaging indicate the JUNQ is not a homogeneous inclusion, but
462 instead consists of an assembly of dynamic membrane-less PQC inclusions called Q-bodies[54, 95],
463 which form in a chaperone-dependent manner early during misfolding. Previously shown to be
464 proximal to the ER, we find they are also close to mitochondria[2,9]. It will be of interest to assess
465 how Q-bodies congregate to form the JUNQ, but perhaps the pathway is akin to the Syntaxin 5-
466 dependent pathway described to traffic Hsp104-associated aggregates [20]. Notably, the Q-bodies
467 and JUNQ exhibit a distinct linear absorption coefficient in cryo-SXT data (Figure 4b-f),
468 suggesting they may be liquid-like phase-separated entities [54].

469 Spatial sorting of misfolded proteins into inclusions is proposed to serve to sequester toxic species
470 away from the cellular milieu and enhance cellular fitness [17, 20, 96]. The convergence of INQ and
471 JUNQ to nuclear-vacuolar contacts may additionally serve to connect spatial PQC to vacuolar
472 clearance, thus providing an alternate route to proteasomal degradation. Of note, vacuolar protein
473 clearance of proteins in both INQ and JUNQ is seen without proteasome inhibitors, as shown using
474 Keima fusions, as well as by immunoblot analyses in *pep4*Δ or *vps4*Δ cells (Figures 1c-d, 2a, c-g,
475 5h, 7c-g). It thus appears that proteasomal and vacuolar clearance do not necessarily function
476 hierarchically for spatial PQC. This raises interesting questions for future studies, including
477 whether they can act on the same pool of PQC substrates, or select their substrates based on distinct
478 chaperone and/or ubiquitin signals [93].

479 Our observation that the INQ can be extruded from the nucleus via the NVJ, indicates a path to
480 clear the nuclear compartment from misfolded proteins even when the proteasome is overloaded
481 or otherwise impaired. The physical tether provided by NVJs previously shown to mediate
482 engulfment of regions of the nuclear membrane into the vacuole, similarly mediates egress of the

483 INQ into the vacuole. This could explain how NVJ disruption leads to INQ extrusion into the
484 cytoplasm. The perinuclear ESCRT-II/III protein Chm7 (CHMP7 in mammals), is involved in
485 this process. Chm7 participates in recruiting nuclear and cytoplasmic PQC compartments to a
486 unique location on the nuclear envelope. While Chm7 is normally diffuse throughout the
487 cytoplasm (Extended Data Fig. 5e). Upon activation Chm7 becomes associated with a unique site
488 in the nuclear envelope upon activation. While the active conformation can be induced by deleting
489 auto-inhibitory helices in the ESCRT-III domain [69], we did not yet identify the mode of activation
490 of Chm7 by PQC inclusions. CHMP7 was previously shown to function in remodeling nuclear
491 envelopes [67], clearance of misassembled nuclear pores [68], egress of herpes virus from the nucleus
492 to the cytosol [97], as well as nuclear envelope sealing and nuclear pore quality control [69]. Our data
493 provides an intriguing link between protein quality control and nuclear envelope quality control.
494 Future studies should determine whether additional forms of microautophagy, such as
495 nucleophagy, ERphagy, piecemeal microautophagy of the nucleus, or selective autophagy of
496 nuclear pore complexes participate in clearance of these PQC compartments.

497 The role for nuclear pores, nuclear-vacuolar contacts and the nuclear envelope in communicating
498 nucleocytoplasmic protein quality control decisions between the nucleus, the cytoplasm and the
499 endolysosomal system places spatial PQC in the larger context of cellular organization and inter-
500 organellar communication [98]. This idea is particularly intriguing given the link between nuclear
501 pore dysfunction and aging, lamin progeria mutants and neurodegenerative diseases such as
502 Huntington's disease, Amyotrophic Lateral Sclerosis and Frontal Temporal Dementia, which are
503 all characterized by nuclear pore dysfunction and altered nucleocytoplasmic trafficking [31, 34, 35, 99-
504 102]. Our findings raise the possibility that compromising nucleocytoplasmic trafficking leads to
505 impaired misfolded protein clearance contributing to further cellular dysfunction. A better

506 understanding of these pathways may provide fundamental insights into the critical biological
507 process of protein quality control and point to avenues to ameliorate a large range of human
508 disorders.

509

510 **MAIN REFERENCES**

511 1. Hartl, F.U., Bracher, A. & Hayer-Hartl, M. Molecular chaperones in protein folding and
512 proteostasis. *Nature* **475**, 324-332 (2011).
513 2. Needham, P.G., Guerriero, C.J. & Brodsky, J.L. Chaperoning Endoplasmic Reticulum-
514 Associated Degradation (ERAD) and Protein Conformational Diseases. *Cold Spring*
515 *Harb Perspect Biol* **11** (2019).
516 3. Balchin, D., Hayer-Hartl, M. & Hartl, F.U. In vivo aspects of protein folding and quality
517 control. *Science* **353**, aac4354 (2016).
518 4. Sontag, E.M., Samant, R.S. & Frydman, J. Mechanisms and Functions of Spatial Protein
519 Quality Control. *Annu Rev Biochem* (2017).
520 5. Pohl, C. & Dikic, I. Cellular quality control by the ubiquitin-proteasome system and
521 autophagy. *Science* **366**, 818-822 (2019).
522 6. Finley, D. & Prado, M.A. The Proteasome and Its Network: Engineering for Adaptability.
523 *Cold Spring Harb Perspect Biol* **12** (2020).
524 7. Alberti, S. & Hyman, A.A. Are aberrant phase transitions a driver of cellular aging?
525 *Bioessays* (2016).
526 8. Ano Bom, A.P. *et al.* Mutant p53 aggregates into prion-like amyloid oligomers and
527 fibrils: implications for cancer. *J Biol Chem* **287**, 28152-28162 (2012).
528 9. Douglas, P.M. & Dillin, A. Protein homeostasis and aging in neurodegeneration. *J Cell*
529 *Biol* **190**, 719-729 (2010).
530 10. De Mattos, E.P. *et al.* Protein Quality Control Pathways at the Crossroad of
531 Synucleinopathies. *J Parkinsons Dis* **10**, 369-382 (2020).
532 11. Kaganovich, D., Kopito, R. & Frydman, J. Misfolded proteins partition between two
533 distinct quality control compartments. *Nature* **454**, 1088-1095 (2008).
534 12. Dillin, A. & Cohen, E. Ageing and protein aggregation-mediated disorders: from
535 invertebrates to mammals. *Philos Trans R Soc Lond B Biol Sci* **366**, 94-98 (2011).
536 13. Balch, W.E., Morimoto, R.I., Dillin, A. & Kelly, J.W. Adapting proteostasis for disease
537 intervention. *Science* **319**, 916-919 (2008).
538 14. Reichmann, D., Voth, W. & Jakob, U. Maintaining a Healthy Proteome during Oxidative
539 Stress. *Mol Cell* **69**, 203-213 (2018).
540 15. Morales-Polanco, F., Lee, J.H., Barbosa, N.M. & Frydman, J. Cotranslational
541 Mechanisms of Protein Biogenesis and Complex Assembly in Eukaryotes. *Annu Rev*
542 *Biomed Data Sci* **5**, 67-94 (2022).

543 16. Specht, S., Miller, S.B., Mogk, A. & Bukau, B. Hsp42 is required for sequestration of
544 protein aggregates into deposition sites in Saccharomyces cerevisiae. *J Cell Biol* **195**,
545 617-629 (2011).
546 17. Escusa-Toret, S., Vonk, W.I. & Frydman, J. Spatial sequestration of misfolded proteins
547 by a dynamic chaperone pathway enhances cellular fitness during stress. *Nat Cell Biol*
548 (2013).
549 18. Miller, S.B. *et al.* Compartment-specific aggregases direct distinct nuclear and
550 cytoplasmic aggregate deposition. *EMBO J* **34**, 778-797 (2015).
551 19. Weisberg, S.J. *et al.* Compartmentalization of superoxide dismutase 1 (SOD1G93A)
552 aggregates determines their toxicity. *Proc Natl Acad Sci U S A* **109**, 15811-15816 (2012).
553 20. Babazadeh, R. *et al.* Syntaxin 5 Is Required for the Formation and Clearance of Protein
554 Inclusions during Proteostatic Stress. *Cell Rep* **28**, 2096-2110 e2098 (2019).
555 21. Nollen, E.A. *et al.* Dynamic changes in the localization of thermally unfolded nuclear
556 proteins associated with chaperone-dependent protection. *Proc Natl Acad Sci U S A* **98**,
557 12038-12043 (2001).
558 22. Yasuda, S. *et al.* Stress- and ubiquitylation-dependent phase separation of the
559 proteasome. *Nature* **578**, 296-300 (2020).
560 23. Polling, S. *et al.* Misfolded polyglutamine, polyalanine, and superoxide dismutase 1
561 aggregate via distinct pathways in the cell. *J Biol Chem* **289**, 6669-6680 (2014).
562 24. Park, J.H. *et al.* Amyotrophic lateral sclerosis-related mutant superoxide dismutase 1
563 aggregates inhibit 14-3-3-mediated cell survival by sequestration into the JUNQ
564 compartment. *Hum Mol Genet* **26**, 3615-3629 (2017).
565 25. McClellan, A.J., Scott, M.D. & Frydman, J. Folding and quality control of the VHL
566 tumor suppressor proceed through distinct chaperone pathways. *Cell* **121**, 739-748
567 (2005).
568 26. Gupta, R. *et al.* Firefly luciferase mutants as sensors of proteome stress. *Nat Methods* **8**,
569 879-884 (2011).
570 27. Samant, R.S., Livingston, C.M., Sontag, E.M. & Frydman, J. Distinct proteostasis circuits
571 cooperate in nuclear and cytoplasmic protein quality control. *Nature* **563**, 407-411
572 (2018).
573 28. Popken, P., Ghavami, A., Onck, P.R., Poolman, B. & Veenhoff, L.M. Size-dependent
574 leak of soluble and membrane proteins through the yeast nuclear pore complex. *Mol Biol*
575 *Cell* **26**, 1386-1394 (2015).
576 29. Amm, I. & Wolf, D.H. Molecular mass as a determinant for nuclear San1-dependent
577 targeting of misfolded cytosolic proteins to proteasomal degradation. *FEBS Lett* **590**,
578 1765-1775 (2016).
579 30. Timney, B.L. *et al.* Simple rules for passive diffusion through the nuclear pore complex.
580 *J Cell Biol* **215**, 57-76 (2016).
581 31. Woerner, A.C. *et al.* Cytoplasmic protein aggregates interfere with nucleocytoplasmic
582 transport of protein and RNA. *Science* **351**, 173-176 (2016).
583 32. Park, S.H. *et al.* PolyQ Proteins Interfere with Nuclear Degradation of Cytosolic Proteins
584 by Sequestering the Sis1p Chaperone. *Cell* **154**, 134-145 (2013).
585 33. Neuber, A. *et al.* Nuclear export receptor Xpo1/Crm1 is physically and functionally
586 linked to the spindle pole body in budding yeast. *Mol Cell Biol* **28**, 5348-5358 (2008).
587 34. Grima, J.C. *et al.* Mutant Huntingtin Disrupts the Nuclear Pore Complex. *Neuron* **94**, 93-
588 107 e106 (2017).

589 35. Gasset-Rosa, F. *et al.* Polyglutamine-Expanded Huntingtin Exacerbates Age-Related
590 Disruption of Nuclear Integrity and Nucleocytoplasmic Transport. *Neuron* **94**, 48-57 e44
591 (2017).
592 36. Wente, S.R. & Blobel, G. A temperature-sensitive NUP116 null mutant forms a nuclear
593 envelope seal over the yeast nuclear pore complex thereby blocking nucleocytoplasmic
594 traffic. *J Cell Biol* **123**, 275-284 (1993).
595 37. Chen, L. *et al.* Sts1 plays a key role in targeting proteasomes to the nucleus. *J Biol Chem*
596 **286**, 3104-3118 (2011).
597 38. Takeda, K. & Yanagida, M. Regulation of nuclear proteasome by Rhp6/Ubc2 through
598 ubiquitination and destruction of the sensor and anchor Cut8. *Cell* **122**, 393-405 (2005).
599 39. Tatebe, H. & Yanagida, M. Cut8, essential for anaphase, controls localization of 26S
600 proteasome, facilitating destruction of cyclin and Cut2. *Curr Biol* **10**, 1329-1338 (2000).
601 40. Romero-Perez, L., Chen, L., Lambertson, D. & Madura, K. Sts1 can overcome the loss of
602 Rad23 and Rpn10 and represents a novel regulator of the ubiquitin/proteasome pathway.
603 *J Biol Chem* **282**, 35574-35582 (2007).
604 41. Lord, C.L. & Wente, S.R. Nuclear envelope-vacuole contacts mitigate nuclear pore
605 complex assembly stress. *J Cell Biol* **219** (2020).
606 42. Crisp, M. *et al.* Coupling of the nucleus and cytoplasm: role of the LINC complex. *J Cell*
607 *Biol* **172**, 41-53 (2006).
608 43. Aitchison, J.D., Blobel, G. & Rout, M.P. Nup120p: a yeast nucleoporin required for NPC
609 distribution and mRNA transport. *J Cell Biol* **131**, 1659-1675 (1995).
610 44. Heath, C.V. *et al.* Nuclear pore complex clustering and nuclear accumulation of poly(A)+
611 RNA associated with mutation of the Saccharomyces cerevisiae RAT2/NUP120 gene. *J*
612 *Cell Biol* **131**, 1677-1697 (1995).
613 45. Ader, C. *et al.* Amyloid-like interactions within nucleoporin FG hydrogels. *Proc Natl*
614 *Acad Sci U S A* **107**, 6281-6285 (2010).
615 46. Strawn, L.A., Shen, T., Shulga, N., Goldfarb, D.S. & Wente, S.R. Minimal nuclear pore
616 complexes define FG repeat domains essential for transport. *Nat Cell Biol* **6**, 197-206
617 (2004).
618 47. Parkinson, D.Y. *et al.* Nanoimaging cells using soft X-ray tomography. *Methods Mol*
619 *Biol* **950**, 457-481 (2013).
620 48. Le Gros, M.A. *et al.* Biological soft X-ray tomography on beamline 2.1 at the Advanced
621 Light Source. *J Synchrotron Radiat* **21**, 1370-1377 (2014).
622 49. Larabell, C.A. & Nugent, K.A. Imaging cellular architecture with X-rays. *Curr Opin*
623 *Struct Biol* **20**, 623-631 (2010).
624 50. Le Gros, M.A., McDermott, G., Uchida, M., Knoechel, C.G. & Larabell, C.A. High-
625 aperture cryogenic light microscopy. *J Microsc* **235**, 1-8 (2009).
626 51. Ekman, A. *et al.* Putting Molecules in the Picture: Using Correlated Light Microscopy
627 and Soft X-Ray Tomography to Study Cells, in *Synchrotron Light Sources and Free-*
628 *Electron Lasers: Accelerator Physics, Instrumentation and Science Applications*. (eds. E.
629 Jaeschke, S. Khan, J.R. Schneider & J.B. Hastings) 1-32 (Springer International
630 Publishing, Cham; 2019).
631 52. Ekman, A.A. *et al.* Mesoscale imaging with cryo-light and X-rays: Larger than molecular
632 machines, smaller than a cell. *Biol Cell* **109**, 24-38 (2017).
633 53. Huh, W.K. *et al.* Global analysis of protein localization in budding yeast. *Nature* **425**,
634 686-691 (2003).

635 54. Wu, G.H. *et al.* Multi-scale 3D Cryo-Correlative Microscopy for Vitrified Cells.
636 *Structure* **28**, 1231-1237.e1233 (2020).
637 55. Schuler, M.H. *et al.* Miro1-mediated mitochondrial positioning shapes intracellular
638 energy gradients required for cell migration. *Mol Biol Cell* **28**, 2159-2169 (2017).
639 56. Frottin, F. *et al.* The nucleolus functions as a phase-separated protein quality control
640 compartment. *Science* **365**, 342-347 (2019).
641 57. Velazquez, J.M. & Lindquist, S. hsp70: nuclear concentration during environmental
642 stress and cytoplasmic storage during recovery. *Cell* **36**, 655-662 (1984).
643 58. Falahati, H., Pelham-Webb, B., Blythe, S. & Wieschaus, E. Nucleation by rRNA Dictates
644 the Precision of Nucleolus Assembly. *Curr Biol* **26**, 277-285 (2016).
645 59. Azkanaz, M. *et al.* Protein quality control in the nucleolus safeguards recovery of
646 epigenetic regulators after heat shock. *Elife* **8** (2019).
647 60. Pan, X. *et al.* Nucleus-vacuole junctions in Saccharomyces cerevisiae are formed through
648 the direct interaction of Vac8p with Nvj1p. *Mol Biol Cell* **11**, 2445-2457 (2000).
649 61. Kohlwein, S.D. *et al.* Tsc13p is required for fatty acid elongation and localizes to a novel
650 structure at the nuclear-vacuolar interface in Saccharomyces cerevisiae. *Mol Cell Biol* **21**,
651 109-125 (2001).
652 62. Levine, T.P. & Munro, S. Dual targeting of Osh1p, a yeast homologue of oxysterol-
653 binding protein, to both the Golgi and the nucleus-vacuole junction. *Mol Biol Cell* **12**,
654 1633-1644 (2001).
655 63. Kvam, E. & Goldfarb, D.S. Structure and function of nucleus-vacuole junctions: outer-
656 nuclear-membrane targeting of Nvj1p and a role in tryptophan uptake. *J Cell Sci* **119**,
657 3622-3633 (2006).
658 64. Kvam, E. & Goldfarb, D.S. Nucleus-vacuole junctions and piecemeal microautophagy of
659 the nucleus in S. cerevisiae. *Autophagy* **3**, 85-92 (2007).
660 65. Roberts, P. *et al.* Piecemeal microautophagy of nucleus in Saccharomyces cerevisiae.
661 *Mol Biol Cell* **14**, 129-141 (2003).
662 66. Krick, R. *et al.* Piecemeal microautophagy of the nucleus requires the core
663 macroautophagy genes. *Mol Biol Cell* **19**, 4492-4505 (2008).
664 67. von Appen, A. *et al.* LEM2 phase separation promotes ESCRT-mediated nuclear
665 envelope reformation. *Nature* **582**, 115-118 (2020).
666 68. Thaller, D.J. & Patrick Lusk, C. Fantastic nuclear envelope herniations and where to find
667 them. *Biochem Soc Trans* **46**, 877-889 (2018).
668 69. Webster, B.M. *et al.* Chm7 and Heh1 collaborate to link nuclear pore complex quality
669 control with nuclear envelope sealing. *EMBO J* **35**, 2447-2467 (2016).
670 70. Thaller, D.J. *et al.* An ESCRT-LEM protein surveillance system is poised to directly
671 monitor the nuclear envelope and nuclear transport system. *Elife* **8** (2019).
672 71. Babst, M., Odorizzi, G., Estepa, E.J. & Emr, S.D. Mammalian tumor susceptibility gene
673 101 (TSG101) and the yeast homologue, Vps23p, both function in late endosomal
674 trafficking. *Traffic* **1**, 248-258 (2000).
675 72. Katzmann, D.J., Babst, M. & Emr, S.D. Ubiquitin-dependent sorting into the
676 multivesicular body pathway requires the function of a conserved endosomal protein
677 sorting complex, ESCRT-I. *Cell* **106**, 145-155 (2001).
678 73. Herrador, A., Léon, S., Haguenauer-Tsapis, R. & Vincent, O. A mechanism for protein
679 monoubiquitination dependent on a trans-acting ubiquitin-binding domain. *J Biol Chem*
680 **288**, 16206-16211 (2013).

681 74. Stack, J.H., Herman, P.K., Schu, P.V. & Emr, S.D. A membrane-associated complex
682 containing the Vps15 protein kinase and the Vps34 PI 3-kinase is essential for protein
683 sorting to the yeast lysosome-like vacuole. *EMBO J* **12**, 2195-2204 (1993).
684 75. Herman, P.K. & Emr, S.D. Characterization of VPS34, a gene required for vacuolar
685 protein sorting and vacuole segregation in Saccharomyces cerevisiae. *Mol Cell Biol* **10**,
686 6742-6754 (1990).
687 76. Burda, P., Padilla, S.M., Sarkar, S. & Emr, S.D. Retromer function in endosome-to-Golgi
688 retrograde transport is regulated by the yeast Vps34 PtdIns 3-kinase. *J Cell Sci* **115**,
689 3889-3900 (2002).
690 77. Slessareva, J.E., Routt, S.M., Temple, B., Bankaitis, V.A. & Dohlman, H.G. Activation
691 of the phosphatidylinositol 3-kinase Vps34 by a G protein alpha subunit at the endosome.
692 *Cell* **126**, 191-203 (2006).
693 78. Henne, W.M., Stenmark, H. & Emr, S.D. Molecular mechanisms of the membrane
694 sculpting ESCRT pathway. *Cold Spring Harb Perspect Biol* **5** (2013).
695 79. Hurley, J.H. & Hanson, P.I. Membrane budding and scission by the ESCRT machinery:
696 it's all in the neck. *Nat Rev Mol Cell Biol* **11**, 556-566 (2010).
697 80. Katayama, H., Kogure, T., Mizushima, N., Yoshimori, T. & Miyawaki, A. A sensitive
698 and quantitative technique for detecting autophagic events based on lysosomal delivery.
699 *Chem Biol* **18**, 1042-1052 (2011).
700 81. Bialecka-Fornal, M., Makushok, T. & Rafelski, S.M. A Review of Fluorescent Proteins
701 for Use in Yeast. *Methods Mol Biol* **1369**, 309-346 (2016).
702 82. Sitron, C.S., Park, J.H., Giafaglione, J.M. & Brandman, O. Aggregation of CAT tails
703 blocks their degradation and causes proteotoxicity in S. cerevisiae. *PLoS One* **15**,
704 e0227841 (2020).
705 83. Schuck, S., Gallagher, C.M. & Walter, P. ER-phagy mediates selective degradation of
706 endoplasmic reticulum independently of the core autophagy machinery. *J Cell Sci* **127**,
707 4078-4088 (2014).
708 84. Haupts, U., Maiti, S., Schwille, P. & Webb, W.W. Dynamics of fluorescence fluctuations
709 in green fluorescent protein observed by fluorescence correlation spectroscopy. *Proc Natl*
710 *Acad Sci U S A* **95**, 13573-13578 (1998).
711 85. Shinoda, H., Shannon, M. & Nagai, T. Fluorescent Proteins for Investigating Biological
712 Events in Acidic Environments. *Int J Mol Sci* **19** (2018).
713 86. Klionsky, D.J. *et al.* Guidelines for the use and interpretation of assays for monitoring
714 autophagy (4th edition). *Autophagy* **17**, 1-382 (2021).
715 87. Eising, S. *et al.* A lysosomal biogenesis map reveals the cargo spectrum of yeast vacuolar
716 protein targeting pathways. *J Cell Biol* **221** (2022).
717 88. Waite, K.A., De-La Mota-Peynado, A., Vontz, G. & Roelofs, J. Starvation Induces
718 Proteasome Autophagy with Different Pathways for Core and Regulatory Particles. *J Biol*
719 *Chem* **291**, 3239-3253 (2016).
720 89. Kvam, E. & Goldfarb, D.S. Nvj1p is the outer-nuclear-membrane receptor for oxysterol-
721 binding protein homolog Osh1p in Saccharomyces cerevisiae. *J Cell Sci* **117**, 4959-4968
722 (2004).
723 90. Vida, T.A. & Emr, S.D. A new vital stain for visualizing vacuolar membrane dynamics
724 and endocytosis in yeast. *J Cell Biol* **128**, 779-792 (1995).
725 91. Thorn, K. Genetically encoded fluorescent tags. *Mol Biol Cell* **28**, 848-857 (2017).

726 92. Costantini, L.M. *et al.* A palette of fluorescent proteins optimized for diverse cellular
727 environments. *Nat Commun* **6**, 7670 (2015).
728 93. Schneider, K.L. *et al.* Using reporters of different misfolded proteins reveals differential
729 strategies in processing protein aggregates. *J Biol Chem* **298**, 102476 (2022).
730 94. Amm, I., Sommer, T. & Wolf, D.H. Protein quality control and elimination of protein
731 waste: the role of the ubiquitin-proteasome system. *Biochim Biophys Acta* **1843**, 182-196
732 (2014).
733 95. Eisele, F. *et al.* An Hsp90 co-chaperone links protein folding and degradation and is part
734 of a conserved protein quality control. *Cell Rep* **35**, 109328 (2021).
735 96. Arrasate, M., Mitra, S., Schweitzer, E.S., Segal, M.R. & Finkbeiner, S. Inclusion body
736 formation reduces levels of mutant huntingtin and the risk of neuronal death. *Nature* **431**,
737 805-810 (2004).
738 97. Kumar, B. *et al.* ESCRT-I Protein Tsg101 Plays a Role in the Post-macropinocytic
739 Trafficking and Infection of Endothelial Cells by Kaposi's Sarcoma-Associated
740 Herpesvirus. *PLoS Pathog* **12**, e1005960 (2016).
741 98. Gottschling, D.E. & Nystrom, T. The Upsides and Downsides of Organelle
742 Interconnectivity. *Cell* **169**, 24-34 (2017).
743 99. Zhang, K. *et al.* The C9orf72 repeat expansion disrupts nucleocytoplasmic transport.
744 *Nature* **525**, 56-61 (2015).
745 100. Fallini, C., Khalil, B., Smith, C.L. & Rossoll, W. Traffic jam at the nuclear pore: All
746 roads lead to nucleocytoplasmic transport defects in ALS/FTD. *Neurobiol Dis* **140**,
747 104835 (2020).
748 101. Shang, J. *et al.* Aberrant distributions of nuclear pore complex proteins in ALS mice and
749 ALS patients. *Neuroscience* **350**, 158-168 (2017).
750 102. Chou, C.C. *et al.* TDP-43 pathology disrupts nuclear pore complexes and
751 nucleocytoplasmic transport in ALS/FTD. *Nat Neurosci* **21**, 228-239 (2018).

752

753

754 **FIGURE TITLES AND LEGENDS**

755 **Figure 1: The INQ and JUNQ are separate nuclear and cytoplasmic PQC compartments.**

756 (a) Schematic showing nuclear and cytoplasmic misfolded proteins could be sequestered into
757 separate compartments or the cytoplasmic misfolded proteins could be imported into the nucleus
758 and sequestered into the nuclear PQC compartment INQ. (b) Experimental schematic.
759 Temperature sensitive Luciferase is properly folded at 25 °C. Heat shock at 37 °C leads to
760 unfolding and sequestration of the protein. Degradation of the unfolded and sequestered proteins
761 can be blocked by treatment with the proteasome inhibitor MG132. (c, d) Live-cell time-lapse
762 fluorescence microscopy of WT cells expressing NLS-LuciTs (c) or NES-LuciTs (d) at 37 °C,
763 treated with DMSO (top) or 100μM MG132 (bottom). Representative still frames at the times
764 shown. Scale bars are 1μm. (e, f) Representative SIM images of WT cells expressing NLS-LuciTs
765 (e) or NLS-VHL (f) after 2 hr at 37 °C and treated with 100μM MG132. NLS-LuciTs and NLS-
766 VHL are shown in green, nuclear pores in gold, and Hoechst counterstain in blue. Scale bars are
767 1μm. Line intensity profiles indicate relative locations of subcellular compartments to Nups and
768 DNA. (g, h) Representative SIM images of WT cells expressing NES-LuciTs (g) and NES-VHL
769 (h) after 2 hr at 37 °C and treated with 100μM MG132. NES-LuciTs and NES-VHL are shown in
770 purple, nuclear pores in gold, and Hoechst counterstain in blue. Scale bars are 1μm. Line intensity
771 profiles indicate relative locations of subcellular compartments to Nups and DNA.

772 **Figure 2: Nuclear entry of misfolded proteins is not required for clearance.**

773 (a) Representative SIM images of WT cells expressing Ubc9Ts-GFP after 2h at 37 °C treated with
774 DMSO (a) or 100μM MG132 (b). Ubc9Ts-GFP is shown in green, nuclear pores in gold, and
775 Hoechst counterstain in blue. Scale bars are 1μm. Line intensity profiles indicate relative locations
776 of subcellular compartments to Nups and DNA. (c) Representative confocal fluorescence
777 microscopy images of cells expressing sGFP with DMSO (control), 100μM MG132 treatment, co-
778 expression of mHTT97QΔP or 200nM Leptomycin B treatment. Ratio of cytoplasmic:nuclear
779 fluorescence is shown in d. Kruskal-Wallis test with Dunn's multiple comparisons test was
780 performed using Prism. Adjusted p value of No Treatment vs. MG132 is 0.0014, No Treatment
781 vs. 97QΔP is 0.0027 and No Treatment vs. LMB is <0.0001. A minimum of 500 cells per condition
782 from 3 biologically independent experiments were analyzed. All scale bars are 1μm. (e) Schematic
783 illustrating the clearance of Ubc9Ts in WT yeast. (*ii*) Timeline of treatments for clearance
784 measurements with shift to 37 °C 60 minutes before initiation of the measurements. (f) Schematic
785 illustrating the *nup116-5* yeast have sealed nuclear pores at 37 °C, thus blocking
786 nucleocytoplasmic trafficking. (*ii*) Densitometric quantification of Western blot bands (*iii*)
787 measuring the amount of Ubc9Ts-EGFP remaining in shut-off experiment of WT vs *nup116*-5
788 cells relative to $t = 0$ (mean ± s.e.m. from three biologically independent experiments) fitted with
789 a one-phase decay non-linear fit regression line. (g) Schematic illustrating the *sts1-2* yeast do not
790 translocate proteasomes to the nucleus at 37 °C. (*ii*) Densitometric quantification of Western blot
791 bands (iii) measuring the amount of Ubc9Ts-EGFP remaining in shut-off experiment of WT vs
792 sts1-2 cells relative to t = 0 (mean ± s.e.m. from three biologically independent experiments) fitted
793 with a one-phase decay non-linear fit regression line.

794 **Figure 3: INQ and JUNQ home to similar location on each side of the nuclear envelope via a**
795 **cytoplasmic signal linked to nuclear pores.**
796 WT cells co-expressing NLS-GFP-LuciTs and NES-DsRed-LuciTs were shifted to 37 °C, treated
797 with 100μM MG132 and monitored by live cell time-lapse fluorescence. Representative still
798 frames at the times shown. Scale bar is 1μm. (b) Graph of the distance between the INQ and JUNQ
799 compartments by particle tracking of inclusions from cell shown in (a) over the time course of the
800 experiment. The slight variations of tethered distance between 60 and 90 minutes is likely due to
801 the relative migration of one of the inclusions around a cellular structure as this fluctuation can be
802 seen at different times post-tethering in other cells (not shown). (c) Representative SIM image
803 taken of cells co-expressing NLS-EGFP-LuciTs and NES-DsRed-LuciTs after 2 hr at 37 °C and
804 treated with 100μM MG132. NLS-fusion proteins are shown in green, NES-fusion proteins in
805 purple, nuclear pores in gold, and Hoechst counterstain in blue. Scale bar is 1μm. Line intensity
806 profiles indicate relative locations of subcellular compartments and Nups. (d) Representative
807 confocal microscopy images taken of WT and 3 separate *nup120Δ* yeast cells expressing NES-
808 LuciTs (*i*), NLS-LuciTs (*ii*) or co-expressing NLS- and NES-LuciTs (*iii*) after 2 hr at 37 °C. NLS-
809 LuciTs is shown in green, NES-LuciTs in purple, nuclear pores in gold, and Hoechst counterstain
810 in blue. Scale bar is 1μm. Schematics on the right summarize the findings of the data. (e) Schematic
811 summarizing the data that the JUNQ localizes to the nuclear pores. A signal is transmitted through
812 or near the nuclear pores to recruit the INQ to the same location, resulting in the homing of the 2
813 compartments.

814 **Figure 4: INQ resides near the nucleolus, JUNQ is surrounded by mitochondria, and both**
815 **compartments home into the Nuclear-Vacuolar Junction.**
816 (a) Unfixed, intact yeast cells are frozen in a capillary tube and imaged by fluorescence microscopy
817 and then X-ray tomography. The linear absorption coefficients are measured from the tomography
818 data and used to identify the subcellular compartments and organelles. The fluorescence images
819 are then correlated to the X-ray tomography data and 3D reconstructions of the subcellular
820 components are generated to determine the cellular context of the PQC compartments. (b) WT
821 cells co-expressing Hsp104-GFP from the endogenous locus and HTT97QP-ChFP after 30 mins
822 at 37 °C. (left) X-ray tomograms without and with fluorescence overlay to indicate sites of
823 Hsp104-GFP positive inclusions and HTT97QP-ChFP inclusion. (right) Table of Linear
824 Absorption Coefficient (LAC) values from the X-ray tomograms used to annotate the images and
825 generate a 3D reconstruction shown in panel c. (c) 3D reconstruction of fluorescence correlated
826 X-ray tomograms showing the JUNQ residing 450nm outside the barrier of the nucleus as defined
827 by the location of the nuclear envelope in the X-ray data (inset, top) and the IPOD marked by
828 mHTT (inset, bottom). JUNQ is shown in green, IPOD in orange, nucleus in yellow, mitochondria
829 in cyan, vacuoles in gray, and lipid droplets in white. Scale bar on X-ray 3D reconstruction is 1μm,
830 insets are 0.5μm. (d) 3D reconstruction of X-ray tomograms from cell expressing NES-LuciTs
831 after 90 mins heat shock at 37 °C and treated with 100μM MG132. The Q-bodies can be seen to
832 coalesce into the JUNQ compartment just outside the nuclear boundary (inset ii). The Q-bodies
833 also interact with vacuoles and the site of coalescence into the JUNQ compartment is surrounded
834 by a mitochondrial cage (inset i). Q-bodies and IPOD are shown in purple, nucleus in yellow,
835 mitochondria in cyan, vacuoles in gray, and lipid droplets in white. Scale bar on X-ray 3D
836 reconstruction is 1μm, insets are 0.5μm. (e) Q-bodies can be seen interacting with mitochondria

837 in a separate cell expressing NES-LuciTs. Q-bodies are shown in purple, nucleus in yellow,
838 nucleolus in gold, mitochondria in cyan, and vacuoles in gray. Scale bar on X-ray 3D
839 reconstruction is 1μm, inset is 0.5μm. (f) Same 3D reconstruction of X-ray tomograms from cell
840 expressing NES-LuciTs after 90 mins heat shock at 37 °C as shown in d. Insets are from the same
841 cell rotated 180°. Blue arrows indicate sites where Q-bodies are directly interacting with the
842 vacuoles. Red arrows indicate sites of nuclear-vacuolar junctions. Scale bar on X-ray 3D
843 reconstruction is 1μm, insets are 0.5μm. (g) 3D reconstruction of X-ray tomograms from cell
844 expressing NLS-LuciTs after 90 mins heat shock at 37 °C and treated with 100μM MG132. The
845 INQ resides 400nm from the nucleolus (inset). INQ is shown in green, nucleus in yellow, nucleolus
846 in gold, mitochondria in cyan, and vacuoles in gray. Scale bar on X-ray 3D reconstruction is 1μm,
847 inset is 0.5μm. (h) Schematic illustrating the novel findings of the association between
848 mitochondria and all 3 cytoplasmic PQC compartments, the proximity of the INQ to the nucleolus,
849 the interaction between Q-bodies and the vacuole, and the hypothesized location of the INQ and
850 JUNQ at the nuclear vacuolar junction. The inset highlights two of the component proteins of the
851 NVJ, Nvj1 and Vac8, that are required for Piecemeal Microautophagy of the Nucleus.

852 **Figure 5: JUNQ and INQ converge at the Nuclear-Vacuolar Junction to facilitate clearance.**
853 (a) Endogenously tagged Nvj1-GFP yeast expressing NES—DsRed-LuciTs were shifted to 37 °C
854 and monitored by live cell time-lapse fluorescence microscopy for the times shown. White
855 arrowheads indicate locations of Nvj1 punctum while yellow arrowheads indicate NES-LuciTs
856 punctum. Scale bar is 1μm. Representative SIM images of WT yeast co-expressing NES-DsRed-
857 LuciTs (b) or NLS-DsRed-LuciTs (c) and Nvj1-sfGFP after 2 hr incubation at 37 °C with 100μM
858 MG132. Panel *ii* of both (b) and (c) are insets to better visualize the relative location of the JUNQ
859 and INQ to the Nvj1. Panel *iii* of both (b) and (c) are additional cells to illustrate other phenotypes
860 seen in the experiment. NES-DsRed-LuciTs is shown in purple, NLS-DsRed-LuciTs is shown in
861 green, Nvj1-sfGFP is shown in yellow, and DNA is shown in blue. Scale bars are 1 μm. (d)
862 Representative confocal image of WT yeast expressing Nvj1-sfGFP (shown in yellow) stained
863 with FM4-64 vacuolar dye (shown in cyan). Scale bar is 1μm. (e) Representative SIM image of
864 WT yeast cell co-expressing NLS-DsRed-LuciTs (shown in green) with Nvj1-sfGFP (shown in
865 yellow) after 2 hr incubation at 37 °C with 100μM MG132. The NLS-LuciTs can be seen extruding
866 through the NVJ toward the vacuole. Scale bar is 1μm. (f) WT (top) and *nvj1Δ* (bottom) cells co-
867 expressing NLS-LuciTs and NES-LuciTs were shifted to 37 °C, treated with 100μM MG132 and
868 monitored by live cell time-lapse fluorescence microscopy for the times shown. White arrowheads
869 indicate inclusions of NLS-LuciTs pulled into the cytoplasm. Scale bars are 1μm. (g)
870 Representative confocal images of WT, *nvj1Δ*, and *vac8Δ* yeast co-expressing NLS-EGFP-LuciTs
871 and NES-DsRed-LuciTs after 2 hr at 37 °C and treated with 100μM MG132. NLS-EGFP-LuciTs
872 is shown in green, NES-DsRed-LuciTs in purple, nuclear pores in gold, and Hoechst counterstain
873 in blue. White arrows indicate cytoplasmic localization of NLS-LuciTs. Scale bar is 1μm. (h)
874 Quantitation of the percentage of cells containing inclusions in WT, *nvj1Δ*, and *vac8Δ* yeast co-

875 expressing NLS-EGFP-LuciTs (*i*) and NES-DsRed-LuciTs (*ii*) after 2 hr incubation at 37 °C with
876 100μM MG132. A minimum of 500 cells per condition from 3 biologically independent
877 experiments were counted and unpaired Student's t-tests were performed comparing the deletion
878 strains to WT. P values were adjusted using two-stage linear step-up procedure of Benjamini,
879 Krieger, and Yekutieli with a false discovery rate (Q) of 5%. Adjusted P value for NLS-LuciTs:
880 WT vs *nvj1Δ* is 0.0205, WT vs *vac8Δ* is 0.0406. Adjusted P value for NES-LuciTs: WT vs *nvj1Δ*
881 is 0.013, WT vs *vac8Δ* is 0.0008. (i) Drop tests showing serial dilutions of WT, *nvj1Δ*, and *vac8Δ*
882 yeast at 30 and 37 °C with no treatment and 0.5mg/mL AZC treatment after 72 h growth at
883 indicated temperature. *nvj1Δ* and *vac8Δ* yeast have a growth defect when subjected to proteostatic
884 stress by AZC treatment.

885 **Figure 6: ESCRT-mediated extrusion from the nucleus and clearance.**
886 (a) The ESCRT-II/-III protein Chm7 has been shown to play a role in clearance of defective nuclear
887 pores and nuclear membrane quality control, therefore, it may be involved in the homing of INQ
888 and JUNQ to the NVJ. (*ii*) Representative confocal images of WT yeast co-expressing $Chm7_{OPEN}$-
889 EGFP and either NLS-DsRed-LuciTs (top) or NES-DsRed-LuciTs (bottom) after 2 hr at 37 °C and
890 treated with 100μM MG132. $Chm7_{OPEN}$ is shown in teal, NLS-DsRed-LuciTs in green, NES-
891 DsRed-LuciTs in purple, nuclear pores in gold and Hoechst counterstain in blue. Arrows indicate
892 locations of puncta for each protein. Scale bar is 1μm. (b) Representative confocal images of WT
893 and *chm7Δ* yeast co-expressing NLS-EGFP-LuciTs and NES-DsRed-LuciTs after 120 minutes at
894 37 °C and treated with 100μM MG132. NLS-EGFP-LuciTs is shown in green, NES-DsRed-
895 LuciTs in purple, nuclear pores in gold, and Hoechst counterstain in blue. Arrows indicate
896 locations of puncta for each protein. Scale bar is 1μm. (c) ESCRT-family proteins Vps23, Vps34,
897 and Vps15 may be involved in clearance of INQ and JUNQ. Representative confocal images of

898 WT and *vps23Δ* , *vps34Δ,* and *vps15Δ* yeast co-expressing NLS-EGFP-LuciTs and NES-DsRed-
899 LuciTs after 2 hr at 37 °C and treated with 100μM MG132. NLS-EGFP-LuciTs is shown in green,
900 NES-DsRed-LuciTs in purple, nuclear pores in gold, and Hoechst counterstain in blue. Insets show
901 the budding INQ encapsulated by nuclear pores. Scale bars are 1μm. (d) ESCRTIII proteins and
902 the ATPase Vps4 are known to remodel membranes and could be involved in vacuolar import of
903 PQC compartments. (e) Quantitation of the percentage of cells containing inclusions of NLS- or
904 NES-LuciTs in WT and *vps4Δ* yeast co-expressing NLS-EGFP-LuciTs and NES-DsRed-LuciTs
905 after 2 hr incubation at 37 °C with 100μM MG132. A minimum of 300 cells per condition from 2
906 biologically independent experiments were counted and Student's T tests were performed
907 comparing the deletion strains to WT. P value for WT vs *vps4Δ* NLS-LuciTs is 0.0007, and WT
908 vs *vps4Δ* NES-LuciTs is 0.0018. (f) Representative confocal images of WT and *vps4Δ* yeast co-
909 expressing NLS-EGFP-LuciTs and NES-DsRed-LuciTs after 2 hr at 37 °C and treated with 100μM
910 MG132. NLS-EGFP-LuciTs is shown in green, NES-DsRed-LuciTs in purple, nuclear pores in
911 gold, and Hoechst counterstain in blue. Green arrows indicate cytoplasmic localization of NLS-
912 LuciTs. Scale bar is 1μm.

913

914 **Figure 7: Vacuolar clearance of the INQ and JUNQ**

915 (a) Possible routes of entry into the vacuole for the INQ and JUNQ. (b) Schematic of the LuciTs-
916 Keima experiments. (c) WT cells expressing NLS-2xKeima-LuciTs after 2 hr incubation at 37 °C
917 with 100μM MG132. Over time, fluorescence is seen with excitation in the 589nm channel
918 indicating the NLS-LuciTs has encountered an acidic environment. Inset shows the transition from
919 green to red and a structure leaving the inclusion that is fully red. Scale bars are 5 uM. (d)
920 Representative images of WT cells expressing NES-2xKeima-LuciTs after 2 hr incubation at 37
921 °C with 100μM MG132. Over time, fluorescence is seen with excitation in the 589nm channel
922 indicating the NLS-LuciTs has encountered an acidic environment. Insets show the transition from
923 green to red and a structure leaving the inclusion that is fully red. Scale bars are 5 uM.
924 Representative Western Blots of NLS-GFP-LuciTs (e) and NES-GFP-LuciTs (f) in WT and *pep4Δ*
925 yeast. *pep4Δ* yeast were also treated with 1mM PMSF to completely inhibit vacuolar proteases. A
926 decrease in fragments can be seen in both the NLS- (e) and NES- (f) blots. (g) Densitometric
927 quantification of Western blot bands measuring the amount of full-length LuciTs-GFP remaining
928 in shut-off experiment as well as the fragments generated during clearance. The ratio of fragment
929 intensity to full-length protein is shown in the graph (mean ± s.e.m. from three biologically
930 independent experiments). One-way ANOVA was performed using Prism software followed by
931 Dunnett's multiple comparisons test. Adjusted P value for WT vs *pep4Δ* NLS-LuciTs is 0.0018,
932 and WT vs pep*4Δ* NES-LuciTs is 0.0220. (h) WT, *nvj1Δ*, and *vps4Δ* yeast expressing NLS-GFP-
933 LuciTs were treated with 8uM of FM4-64 and incubated for 2hr at 37 °C with 100μM MG132.
934 Cells were imaged every 5 mins for 90 mins. Scale bar is 1μm.

935

936

937 **Figure 8: Principles of Nuclear and Cytoplasmic spatial protein quality control**Model for
938 vacuolar targeting and clearance of nuclear and cytoplasmic protein inclusions in yeast. (a) Upon
939 heat shock, cytoplasmic and nuclear LuciTs locally misfold, and recruit chaperones and other PQC
940 factors that facilitate the subcellular spatial sequestration on distinct protein quality control
941 inclusions: (b) the Intranuclear Quality Control compartment (INQ) in the nucleus and Q-bodies
942 in the cytoplasm.(c) Q-bodies then coalesce to form the Juxtanuclear Quality Control compartment
943 (JUNQ), and misfolded proteins located in the INQ and the JUNQ can be degraded by the UPS
944 system in the nucleus and the cytoplasm respectively c.ii). (d) Alternatively, under conditions of
945 limited proteasomal activity, INQ and JUNQ can converge on the periphery of the nuclear
946 envelope, a mechanism mediated by the nuclear pores (homing)(e) The homing mechanism could
947 represent a coordinated way to target both inclusions for clearance at the vacuole. (e.ii) Vacuolar
948 mediated clearance of both INQ and JUNQ. ESCRT-family proteins are involved in organizing
949 the INQ and JUNQ for vacuolar degradation.

950 **METHODS**

951 **Time resolved live cell imaging.** BY4741 Cells were grown overnight in raffinose media followed
952 by 4–6 h at 28 °C in galactose media to induce the expression. Cells were then immobilized on
953 concanavalin A-coated coverslips. Samples were washed in glucose media and kept in the same
954 medium by sealing the coverslips to slides with vacuum grease. When indicated, cells were treated
955 10 min before sealing with 100 uMof MG132 (Sigma) before sealing. Images were taken every 15
956 s for 60 min at 37 °C (or room temperature (25 °C)) using a Zeiss Axio Observer.Z1 inverted
957 microscope equipped with X-cite 120 LED light source (Lumen Dynamics), HE GFP/Cy3/DAPI

958 shift free filter sets (Zeiss), a Plan-Apochromat 100x/1.4 oil DIC M27 objective (Zeiss) and a
959 digital Axiocam MRm camera (Zeiss) controlled with the Zen blue software.

960 **Cycloheximide chase of preformed inclusions.** Cells were grown overnight in raffinose media,
961 back diluted to an OD600 of 0.1 in a 10 ml of galactose media and grown at 25 °C for 5 hours to
962 induce expression of both NLS and NES constructs. Cells were then resuspended in 10 ml of
963 glucose media at 100 µM MG132 and incubated for additional 15 min 25 °C and then switched to
964 37 °C for 30 minutes to ensure inclusion formation before CHX chase. Cells were then
965 immobilized on concanavalin deltaT culture dish (Fischer Scientific), washed with prewarmed
966 glucose media and incubated with glucose media supplemented with 100 µM MG132 and
967 50mg/ml of cycloheximide (CHX). Images were taken every 25 s for 120 min at 37 °C as
968 mentioned above.

969 **FM4-64 vacuole labeling.** 10 ml of cells were grown on galactose media to a final OD600 of 0.8
970 at 25°C. Vacuolar dye was added by resuspending the cells on 2 ml of fresh galactose media plus
971 FM4-64 to a final concentration of 8uM, and incubated 30 min at 25°C. For imaging, cells were
972 then resuspended in glucose media at 100uM MG132 and incubated 20 min at 37°C to induce
973 inclusion formation. Cells were adhered on a concanavalin deltaT culture dish and imaged as
974 mentioned above.

975 **Immunostaining.** As in the live-cell imaging assay, cells were grown overnight in raffinose media
976 followed by 4–6 h at 28 °C in galactose media to induce the expression. Then, the cells were heat-
977 shocked at 37 °C in glucose media for 1 h before fixation in 4% paraformaldehyde for 15 mins at
978 37 °C followed by methanol fixation for 20 mins at -20 °C. Immunostaining proceeded as in [1].
979 Briefly, samples were resuspended in sorbitol buffer and spheroplasted in Zymolyase (Zymo) for
980 30 mins at room temperature and further solubilized in 0.1% Triton X-100 for 10 mins. Antibodies

981 are diluted in Buffer WT (1% nonfat dry milk 0.5 mg/ml BSA 200 mM NaCl 50 mM HEPES–
982 KOH (pH 7.5) 1 mM NaN3 0.1% Tween-20) at a 1:500 dilution and incubated 2 hr at room
983 temperature or overnight at 4 °C. Samples are then washed in Buffer WT followed by incubation
984 in secondary antibodies at a 1:1000 dilution for 2 hr at room temperature. Cells were immobilized
985 on poly-lysine coated coverslips and mounted in Prolong Diamond mounting media (with DAPI
986 where indicated) (Thermo-Fisher). Nanobodies against GFP and RFP were conjugated to Alexa
987 Fluor 488 and Alexa Fluor 568 respectively and used to amplify the signal from the fluorescent
988 proteins during the SIM measurements. Anti-Nsp1 antibody from EnCor Biotechnology was used
989 to visualize nuclear pores and Anti-Nsr1 antibody from Abcam was used for staining the nucleolus.

990 **Confocal microscopy.** Confocal microscopy on immunostained samples was performed on a
991 Zeiss LSM 700 inverted confocal microscope with 405, 488, 555 and 639 nm laser lines with Basic
992 Filterset for LSM700 (Zeiss), a Plan-Apochromat 100x/1.4 oil DIC WD=0.17 objective (Zeiss)
993 and a digital Axiocam MRm camera (Zeiss) controlled with the Zen black software. Confocal data
994 sets were deconvolved when indicated using the Zen software with a fast-iterative function.
995 Fluorescence was quantified where indicated using ImageJ software (NIH). The sGFP intensity
996 measurements, were performed as described previously [2]. Briefly, the raw integrated density
997 (herein indicated as intensity) was measured for the nucleus and the whole cell. The intensity value
998 of the nucleus was then divided by the area. The cytoplasmic intensity was calculated by
999 subtracting the nuclear intensity from the whole cell intensity and the cytoplasmic area by
1000 subtracting the nuclear area from the whole cell area. The cytoplasmic intensity was then divided
1001 by the cytoplasmic area. Finally, the ratio of cytoplasmic to nuclear was calculated by dividing the
1002 cytoplasmic intensity per area by the nuclear intensity per area. Statistical analysis was performed
1003 using Prism (GraphPad).

1004 **Super-resolution microscopy**. Structured illumination microscopy (SIM) on immunostained
1005 samples was performed using an OMX V4 Blaze system (Applied Precision, GE Healthcare)
1006 equipped with a 100×/1.40 NA PlanApo oil-immersion objective (Olympus), 405, 488, 568 and
1007 647 nm diode lasers with standard filter sets, and 3 emCCD cameras (Photometrics Evolve 512).
1008 SIM data were acquired with a Z-distance of 125 nm and with 15 images per plane (five phases,
1009 three angles). The raw data was computationally reconstructed using a Wiener (high-frequency)
1010 filter setting of between 0.001 and 0.003 and channel- specific OTFs employing the softWoRx
1011 version 6.5.2 software package (GE Healthcare) to obtain a super-resolution image stack. 3D
1012 reconstructions and line intensity profiles were generated in Volocity version 6.3 (Perkin Elmer).

1013 To construct *NVJ1-sfGFP* strain with integrated sfGFP fusion at the C-terminal, sf*GFP* was
1014 knocked-in via standard PCR-based homologous recombination. The *sfGFP* cassette was
1015 amplified from plasmid GTL-g (Addgene plasmid #81099) with oligonucleotides

1016 5'TAGATGCACAAGTGAACACTGAACAAGCATACTCTCAACCATTTAGATACGCGGC
1017 CGCTCTAGAACTA and

1018 5' TCGCACCTCGTTGTAAGTGACGATGATAACCGAGATGACGGAAATATAGTACA

1019 ATGGAAAAACGCCAGCAACG. The cassette was amplified, separated by electrophoresis, gel
1020 purified and transformed into yeast cells using the lithium acetate method. Correct transformants
1021 were verified by standard PCR using the oligonucleotides NVJ1-VF:
1022 5'GGATACCAGAACAACCTCTTC, NVJ1-VR: 5' ATGCCCGGCGTTATATATTGC, and
1023 LEU2-VF: 5' AGCACGAGCCTCCTTTACCT.

1024 **Keima cloning.** The NLS-Keima-luciTS plasmid was constructed by replacing the GFP moeity
1025 with yeast optimized Keima using a cassette amplified from plasmid pFA6a-link-yomKeima-
1026 Kan (Addgene plasmid #44902) with the oligonucleotides

1027 5'ATGGCTTCTCCTAAGAAGAAACGTAAAGTTATGGTTTCTGTGATCGCTAAACAAAT
1028 GAC and

1029 5'CCATGCAAGCTTGCGCGGATCCGCGCCCTAATAGAGAATGTCTTGCGATAGC.
1030 Similarly, the NES-Keima-luciTS plasmid was created replacing the GFP moity using the
1031 olinucleotides
1032 5'CTCGCACTTAAGTTCGCCGGTTTAGACCTGATGGTTTCTGTGATCGCTAAACAAAT
1033 GAC and
1034 5'CCATGCAAGCTTGCGCGGATCCGCGCCCTAATAGAGAATGTCTTGCGATAGC. To
1035 construct the NLS and NES-2xKeima-luciTS, an additional Keima moeity was created by
1036 inserting a second keima cassette amplified using the oligonucleotides
1037 5'CCATGCAAGCTTGCGCGGATCCGCGCCCTAATAGAGAATGTCTTGCGATAGC and
1038 5'TTCCATGCAAGCTTGCGCGGATCCGCGCCCTAATAGAGAATGTCTTGCGA.

1039 **Live cell LeicaSp8/sSTED microscopy of Keima-tagged inclusions.** Cells were grown as for
1040 time resolve live fluorescent microscopy, adhered on concanavalin deltaT culture dish and
1041 examined at 37 °C for 90 minutes. Representative cells were collected every 5 minutes on a
1042 Leica TCS SP8 inverted sSTED microscope equipped with a 100x/1.40 APO objective and using
1043 the following detection mirror settings: Keima 590-650nm. Cells were sequentially excited using
1044 404nm and 568 nm laser. One representative middle slide was acquired, and images were
1045 deconvolved and background subtracted using Huygens Professional (Scientific Volume
1046 Imaging).

1047 **Xray-tomography**:

1048 **Preparation of Specimen Mounting Capillaries.** Thin-walled glass capillaries were pulled as
1049 described in [3]. After being cut to length, capillaries were dipped in poly-L-lysine (0.01% solution,
1050 Tissue Culture Grade, Sigma Aldrich, St. Louis, MO). Fiducial markers, used to align soft x-ray
1051 projection images to a common axis, were generated by briefly immersing the capillaries a solution

1052 of 100 nm gold nanoparticles (EMGC100, BBI International, Cardiff, CF14 5DX, UK), rinsing
1053 and then drying them in air.

1054 Specimen capillaries for use in correlated imaging experiments were prepared as above and then
1055 dipped in a suspension of red polystyrene microspheres (FluoSpheres Carboxylate-Modified
1056 Microspheres, 0.2 µm, Dark Red Fluorescent (660 excitation/ 680 emission), Life Technologies,
1057 Invitrogen). The polystyrene microspheres were used fiducial markers for the alignment of
1058 fluorescence images to each other and for the co-alignment of soft x-ray and cryo- fluorescence
1059 tomographic reconstructions.

1060 **Specimen Mounting.**1 ml of yeast cells in mid-log phase growth (OD_{600} ~0.5) were pelleted and
1061 re-suspended in ~50µl media. 1µl of this suspension was transferred into a specimen capillary
1062 using a standard micropipette. The capillary contents were immediately cryopreserved by rapid
1063 plunging into liquid propane at 165°C using a custom apparatus. Cryopreserved specimens were
1064 transferred into storage boxes using a home-built cryo-transfer device and stored in a Dewar held
1065 at 77K [3].

1066 **Imaging Cells in the Cryogenic Confocal Light Microscope (CLM).** Specimen capillaries were
1067 transferred cryogenically to a home-built cryogenic spinning disk confocal fluorescence
1068 microscope [4]. Confocal scanning and detection were achieved using a commercial dual spinning
1069 disk head (CSU-X1, Yokogawa, Tokyo, Japan). During imaging, the illumination wavelength was
1070 selected with an acousto-optical tunable filter (AOTF) using an integrated system (Andor Laser
1071 Combiner, Model LC-501A).

1072 **Experimental measurement of the CLM point spread function.** The point spread function of
1073 the cryogenic confocal light microscope was calculated by the methods described in [5].

1074 **Acquisition of Cryogenic Fluorescence Tomography data.** Cryopreserved specimen capillaries
1075 were cryo-transferred to the CLM and aligned with respect to the rotation axis. Through-focus, or
1076 "z-stacks" were taken using a step size of 0.78 μm. For fluorescence tomography, the capillary
1077 was rotated about an axis normal to the objective lens using a motorized goniometer driven by
1078 custom LabView code (National Instruments Corporation, Austin, TX). Each tomographic data
1079 series consisted of 37 through-focus stacks (0° through 360° measured at 10° increments). Once
1080 measurements were completed, the capillary was cryo-transferred back to liquid nitrogen storage
1081 using the cryo-transfer device [5].

1082 **Alignment of through-focus fluorescence stacks using fluorescence fiducials.** Well-isolated
1083 fluorescent fiducials were chosen manually from the raw fluorescence stacks and a three-
1084 dimensional centroid algorithm refined the bead position to sub-pixel accuracy using the software
1085 package Amira (FEI). The fiducial coordinates were used to write a new image stack in MATLAB
1086 containing a spherically-symmetrical representation of the fiducials, which we termed the "fiducial
1087 model". Six parameters were optimized for each alignment: three translations and three rotations
1088 (a rigid affine transformation). By limiting the search space to optimize correspondence between
1089 bead pairs that had been visually verified to be true fiducial correspondences, this alignment
1090 strategy was relatively fast and robust. The entire fluorescence fiducial alignment optimization
1091 process was visualized in Amira. Visualization was helpful for inspecting the results and
1092 troubleshooting rare cases where the optimization settled into a local maximum that was obviously
1093 not the real solution.

1094 **Fluorescence tomographic reconstruction and deconvolution.** Preprocessed, aligned through-
1095 focus stacks were reconstructed into a single object by simply summing the through-focus datasets
1096 (Amira). The effective PSF for tomographic imaging in a specimen capillary was used as the

1097 convolution kernel to deconvolve the fluorescence reconstruction. We used an iterative function
1098 for the deconvolution. The algorithm found the fluorophore distribution that was most likely,
1099 assuming the PSF was spatially invariant, and that image formation followed Poisson statistics.

1100 **Soft x-ray data collection and reconstruction.** Specimens were imaged using a transmission soft
1101 x-ray microscope, operated by the National Center for X-ray Tomography (NCXT), at the
1102 Advanced Light Source of Lawrence Berkeley National Laboratory and reconstructed according
1103 to previously published protocols.

1104 **Correlated Imaging.** Co-alignment of cryogenic fluorescence and soft x-ray tomographic
1105 reconstructions using joint fiducials

1106 Joint fiducials - red fluorescent polystyrene microspheres - visible in both light- and soft x-ray
1107 images were used to guide overlay of the two data types. The alignment process was optimized by
1108 converting the raw fluorescence into a bead model and aligning the fluorescent bead model to the
1109 x-ray reconstruction of the beads using an iterative optimization of the overlay.

1110 **Identification of JUNQ/IPOD in soft x-ray reconstructions.** Segmentation is the process of
1111 computationally isolating, visualizing, and quantifying specific cellular components in a
1112 tomographic reconstruction. Each voxel in an SXT reconstruction is a direct measurement of the
1113 soft x-ray Linear Absorption Coefficient (LAC) at the corresponding location in the cell.
1114 Attenuation of the illumination by the specimen follows Beer's Law. Hence, the LAC values for
1115 identical sized voxels depends solely on the concentration and composition of biomolecules
1116 present. Consequently, water has an order of magnitude lower LAC than carbon-containing
1117 molecules, such as lipids and proteins. LAC values for homogeneous solutions of isolated
1118 biomolecules can also be calculated using tables of known absorption coefficients. For example,

1119 pure water in the form of ice has a calculated LAC of 0.109 μm^{-1} whereas a model protein with the
1120 chemical composition $C_{94}H_{139}N_{24}O_{31}S$ was calculated to have a theoretical LAC of 1.35μm^{-1} [6]. In
1121 practice, most of the voxels in a 50 nm resolution SXT reconstruction of a cell will contain a
1122 heterogeneous mixture of biomolecules. Using SXT data acquired at a single wavelength it is not
1123 possible to distinguish the precise chemical species present. However, at this level of spatial
1124 resolution organelles and other sub-cellular structures are sufficiently similar in their biochemical
1125 composition to allow them to be readily identified from the surrounding cell contents. The
1126 relatively high water content in vacuoles makes them readily distinguishable from organelles with
1127 a greater density of biomolecules, for example, nuclei and mitochondria. Even relatively small
1128 variations in organelle LAC can be distinguished, for example, the boundaries between nuclei and
1129 nucleoli are very clear, as is the distinction between euchromatin and heterochromatin domains in
1130 the nucleus. LACs were calculated, and cells segmented using the protocols described in complete
1131 detail in [3].

1132 Segmentation of the Hsp104-GFP reconstructions, in particular the assignment of the volumes as
1133 JUNQ and IPOD, were guided by correlative fluorescence signal. In other strains, JUNQ and/or
1134 IPOD were assigned based on LAC values established in the Hsp104-GFP study.

1135 **Western blot.** Yeast cultures were grown to mid- log-phase in synthetic complete medium (yeast
1136 nitrogen base, ammonium sulfate, amino acids, 2% raffinose) lacking uracil. Cultures were then
1137 diluted to an OD_{600} of 0.2 in galactose medium (synthetic complete medium with 2% galactose
1138 and 2% raffinose) and grown to an OD_{600} of 0.8. Cultures were then pelleted and resuspended in
1139 glucose medium (synthetic complete medium with 2% glucose) and incubated at either 30 or 37
1140 °C as indicated for the duration of the shut off. Where indicated, cultures were shifted to 37 °C for
1141 1 hour prior to exchange into glucose medium and incubated at 37 °C for the duration of the

1142 glucose shut-off. Cells were pelleted, proteins were extracted with urea and SDS, and protein
1143 concentrations were measured with the bicinchoninic acid protein assay kit (Thermo Fisher
1144 Scientific). Equal amounts of total protein were resolved on Tris-glycine gels (Invitrogen) and
1145 transferred onto nitrocellulose membranes. GFP was detected with mouse anti-GFP antibodies
1146 (Roche), GAPDH was detected with rabbit anti-GAPHD (Genetex), and PGK was detected with
1147 rabbit anti-PGK antibodies (Thermo Fisher Scientific). Secondary antibodies were IRDye 800CW
1148 donkey anti-mouse or IRDye 680RD donkey anti-rabbit and were imaged using the LiCOR
1149 scanner and Image Studio Software.

1150 To assess vacuolar protein degradation, the same procedure as above was followed but the *pep4D*
1151 yeast were treated with 1mM PMSF (Research Products International) during the 37C incubation
1152 step. The samples were then collected and lysed as above. GFP and GAPDH were detected with
1153 the same primary antibodies, but the secondary antibodies were goat anti-mouse HRP conjugated
1154 antibody (Promega Cat #W4021) and goat anti-rabbit HRP conjugated antibody (Promega Cat #
1155 W4011). Blots were detected using Clarity Western ECL Substrate (Bio-Rad Cat# 1705061) and
1156 imaged using the GE Amersham Imager 600.

1157 **Drop test.** Yeast cultures were grown to OD_{600} of 0.6 in YPD or raffinose synthetic complete
1158 medium and then diluted to OD_{600} of 0.1. Four 10-fold serial dilutions were performed in H_2O.
1159 ~2uL of diluted cultures were spotted onto YPD, galactose, or glucose plates using the pin plater.
1160 Plates were incubated at indicated temperatures and imaged every 24 hours for 72 hours.

1161 **Nanobody purification and labeling.** GFP-nanobody was expressed in BL21 Rosetta2 pLysS
1162 cells (Novagen), and DsRed-nanobody (LAM4) was expressed in ArticExpress cells (Agilent
1163 Technologies) overnight at 17 °C and 12 °C respectively. Cells were pelleted (4000XG), washed
1164 with PBS containing 1 mM PMSF and pelleted again. Pellets were resuspended in column buffer

1165 (500 mM NaCl and 50 mM HEPES pH 8 or 50 mM $NaHCO_3$ pH 8.3) with complete protease
1166 inhibitors, PMSF, benzonase and 10 mM imidazole (Lysis buffer) and lysed using an emulsiflex.
1167 Lysates were cleared at 20,000XG for 30 minutes. Nanobodies were purified using nickel resin
1168 by passing cleared lysate over the resin, washing with lysis buffer, followed by column buffer, and
1169 elution with column buffer containing 300 mM imidazole. Elution was concentrated using an
1170 Amicon ultra 3 kD MWCO to less than 2 mL, and further purified by size exclusion using an
1171 SDX75 column (GE Healthcare) equilibrated with 500 mM NaCl, 50 mM $NaHCO_3$, 1 mM DTT.
1172 Labeling was performed by the addition of dyes at a molar ratio of 5:1 dye:nanobody using Alexa
1173 488 NHS (Thermo Fisher Scientific) for the GFP nanobody and Alexa 568 NHS (Thermo Fisher
1174 Scientific) for the DsRed nanobody. Labeling reactions were incubated 1 hr at room temperature
1175 and quenched by addition of Tris-HCl pH 8 to a final concentration of 100 mM. Labeled nanobody
1176 was separated from free dye by size exclusion using an SDX75 column.

1177 **GFP-nanobody cloning**. pDG402, a vector for expression of GFP-nanobody-TEV-6XHis was
1178 generated by PCR amplification of the GFP nanobody using the 5' primer (XbaI GFP nanobody)
1179 AATCTAGAATTTTGTTTAACTTTAAGAAGG and 3' primer (GS link TEV His nanobody)
1180 AAGGATCCTTATCAGTGATGATGGTGGTGATGGGACCCAGATCCACCCTGGAAGTAT
1181 AAATTCTCACCCGAACCTCCGGATGAGGAGACGGTGACCTGGG. The PCR product
1182 was cloned into the pST39 backbone [7] using XbaI and BamHI.

1183 **METHODS REFERENCES**

1184 1 Brickner, D. G., Light, W. & Brickner, J. H. Quantitative localization of chromosomal
1185 loci by immunofluorescence. *Methods Enzymol* **470**, 569-580, doi:10.1016/S0076-
1186 6879(10)70022-7 (2010).

1187 2 Woerner, A. C. *et al.* Cytoplasmic protein aggregates interfere with nucleocytoplasmic
1188 transport of protein and RNA. *Science* **351**, 173-176, doi:10.1126/science.aad2033 (2016).

1189 3 Parkinson, D. Y. *et al.* Nanoimaging cells using soft X-ray tomography. *Methods Mol*
1190 *Biol* **950**, 457-481, doi:10.1007/978-1-62703-137-0_25 (2013).

1191 4 Le Gros, M. A., McDermott, G., Uchida, M., Knoechel, C. G. & Larabell, C. A. High-
1192 aperture cryogenic light microscopy. *J Microsc* **235**, 1-8, doi:10.1111/j.1365-2818.2009.03184.x
1193 (2009).

1194 5 Le Gros, M. A. *et al.* Biological soft X-ray tomography on beamline 2.1 at the Advanced
1195 Light Source. *J Synchrotron Radiat* **21**, 1370-1377, doi:10.1107/s1600577514015033 (2014).

1196 6 Weiss, D. *et al.* Computed tomography of cryogenic biological specimens based on X-ray
1197 microscopic images. *Ultramicroscopy* **84**, 185-197, doi:10.1016/s0304-3991(00)00034-6 (2000).

1198 7 Tan, S. A modular polycistronic expression system for overexpressing protein complexes

1199 in Escherichia coli. *Protein Expr Purif* **21**, 224-234, doi:10.1006/prep.2000.1363 (2001).

1200 **ACKNOWLEDGMENTS**

1201 We thank support of NIH (GM05643319 and AG054407 to JF; F32NS086253 to ES) and Way
1202 Klingler Startup Funds from Marquette University (ES). F.M-P. was supported by The Pew Trusts
1203 in the Biomedical Sciences postdoctoral Award (00034104). Cryo-SXT data were acquired at the
1204 Advanced Light Source of Lawrence Berkeley National Laboratory, a U.S. DOE Office of Science
1205 User Facility. The National Center for X-ray Tomography is supported by NIH (P41GM103445)
1206 and DOE BER (DE-AC02-5CH11231). CAL and MAL were supported by the Gordon and Betty
1207 Moore Foundation Award #3497. The Stanford Cell Sciences Imaging Facility is supported in part
1208 by Award Number 1S10OD01227601 from the National Center for Research Resources (NCRR).
1209 We thank Jon Mulholland and Youngbin Lim from the CSIF for training on the SIM. We are
1210 grateful to Michael Rosbash (Brandeis University), Susan Wente (Vanderbilt University), Kiran
1211 Madura (Rutgers University), and Patrick Lusk (Yale School of Medicine) for providing yeast
1212 strains and Karsten Weis (ETH Zurich), Jodi Nunnari (University of California, Davis), and
1213 Michael P. Rout (Rockefeller University) for plasmids. We thank Katharine Ullman (University
1214 of Utah), Adam Frost (Altos Lab) and Lisbeth Veenhoff (University of Groningen) for discussions

and advice. We are grateful to Carson Trail for support in microscopy data analysis, Margaret Wangeline for assisting with the 2xKeima cloning, Joan Steffan (UC Irvine), Kelly Rainbolt (Stanford University) for discussions and comments on the manuscript, Felipe Serrano for assisting on Figure 8, and the Frydman lab for advice and discussions.

AUTHOR CONTRIBUTIONS

JF and ES conceived the project; ES and F. M-P carried out all experiments; J-HC collected and processed cryo-SXT data; GM carried out cryo-SXT data analysis and modelling; MLG performed cryo-fluorescence data acquisition and correlation with cryo-SXT data and built the microscope used for these experiments. PD analyzed particle tracking data and assisted on statistical analyses. DG cloned the NLS- and NES- luciferase and VHL plasmids. DG and F. M-P generated, purified and labeled the GFP and RFP nanobodies. ES, F. M-P and JF wrote the MS. All authors commented on the final version. JF directed the project.

DECLARATION OF INTERESTS

The authors declare no competing interests.

ADDITIONAL INFORMATION

Supplementary information is available for this paper.

Correspondence and requests for materials should be addressed to Judith Frydman jfrydman@stanford.edu

EXTENDED DATA FIGURE LEGENDS

1235 **Figure ED1: Spatial sequestration occurs during different types of stress with different**

1236 **client proteins.**

1237 (a) Western blot analyses of Gal Shut-off assays showing the clearance of NLS-LuciTs (top) and

1238 NES-LuciTs (bottom) with and without proteasome impairment by 50uM Bortezomib. (b) Drop

1239 test of W303 yeast expressing model proteins without heat shock at 30C (left), with heat shock at

1240 37 °C (middle), and without expression of the plasmids (right). (c) Representative Structured

1241 Illumination super-resolution microscopy images taken of cells expressing NLS-VHL (left) or

1242 NES-VHL (right) after 120 minutes at 37 °C and treated with 100μM MG132. NLS-LuciTs is

1243 shown in green, NES-LuciTs in purple, nuclear pores in gold and Hoechst counterstain in blue.

1244 Scale bars are 1μm.

1245

1246 **Figure ED2: The effect of blocking nucleocytoplasmic transport on Ubc9Ts clearance.**

1247 (a) Quantitation of the percentage of cells containing nuclear or cytoplasmic inclusions in WT
1248 yeast expressing Ubc9Ts-EGFP after 120 minutes at 37 °C with and without treatment with 100μM
1249 MG132. A minimum of 500 cells per condition from 3 biologically independent experiments were
1250 counted and Student's t-tests were performed comparing the WT yeast without MG132 treatment
1251 to WT yeast with MG132 treatment using Prism software. P values were adjusted using two-stage
1252 linear step-up procedure of Benjamini, Krieger and Yekutieli with a Q of 5%. Adjusted P value
1253 for nuclear no MG132 vs. +MG132 is 0.0035 and cytoplasmic no MG132 vs. +MG132 is 0.0011.
1254 (b) Representative Structured Illumination super-resolution microscopy images taken of cells
1255 expressing GFP-VHL after 2 hr at 37 °C with DMSO (left) or with 100μM MG132 (right)
1256 treatment. VHL is shown in green, nuclear pores in gold, and Hoechst counterstain in blue. Scale
1257 bars are 1μm. (c) (left) Schematic illustrating the *nup116-5* yeast have sealed nuclear pores at 37
1258 °C, thus blocking nucleocytoplasmic trafficking. (right) There is no significant difference in half-
1259 life between WT and *nup116-5* yeast. (d) (left) Schematic illustrating the *sts1-2* yeast do not
1260 translocate proteasomes to the nucleus at 37 °C. (right) There is no significant difference in half-
1261 life between WT and *sts1-2* yeast. (c and d) Levels of EGFP were quantified from 3 biologically
1262 independent experiments. Half-life was calculated using Prism.

1263

1264 **Figure ED3: INQ-JUNQ homing does not occur at the LINC, nucleolus, or involve FG**
1265 **repeats of the nuclear pore central channel.**

1266 (a) Graph of the X-Y positions of the INQ and JUNQ compartments by particle tracking of
1267 inclusions from cell shown in Figure 2a over the time course of the experiment. (b) Representative
1268 confocal image taken of cells co-expressing NLS-EGFP-VHL and NES-DsRed-VHL after 2 hr at
1269 37 °C and treated with 100μM MG132. NLS-fusion proteins are shown in green, NES-fusion
1270 proteins in purple, nuclear pores in gold, and Hoechst counterstain in blue. Scale bar is 1μm. (c)
1271 Representative confocal fluorescence microscopy images taken of cells co-expressing NLS-
1272 EGFP-LuciTs and NES-DsRed-LuciTs (left) after 2 hr at 37 °C and treated with 100μM MG132.
1273 NLS-LuciTs is shown in green, NES-LuciTs in purple, nucleolus (Nsr1) in gold and Hoechst
1274 counterstain in blue. (right) Line intensity profile showing distance between nucleolus and homed
1275 INQ/JUNQ. Scale bars are 1μm. (d) (left) schematic of Mps3 component of LINC complex linking
1276 inner and outer nuclear membranes. (right) Representative widefield fluorescence microscopy
1277 images taken of cells co-expressing endogenously tagged Mps3-EGFP and NES-DsRed-LuciTs
1278 after 120 minutes at 37 °C with and without treatment with 100μM MG132. White arrowheads
1279 indicate locations of Mps3 puncta while yellow arrowheads indicate NES-LuciTs puncta. Scale
1280 bars are 1μm. (e) WT (top) and *nupΔFG* (bottom) cells co-expressing NLS-LuciTs and NES-
1281 LuciTs were shifted to 37 °C and monitored by live cell time-lapse fluorescence microscopy for
1282 the times shown. Scale bars are 1μm.

1283

1284 **Figure ED4: Detailed representation of the cryo-SXT workflow and interactions between**
1285 **mitochondria and cytoplasmic PQC compartments.**
1286 (a) Optical path through the specimen. Key: COL, cryogenic objective lens; SS, specimen stage;
1287 SP, specimen port; MG, motorized goniometer; CIM, cryogenic immersion fluid; CCL, low
1288 magnification cryogenic objective; CS, cryogenic specimen; CIE, cryogenic imaging
1289 environment; AP, adapter port; AW, a heated, angled anti-reflection window. (b) Alignment of
1290 fluorescence and soft x-ray tomographic data using fiducial markers. (c) A representative confocal
1291 image of the spatial relationship between the INQ and nucleolus. NLS-LuciTs (INQ) is shown in
1292 green, nucleolus in gold, and Hoechst counterstain in blue. Scale bar is 1μm. (d) The interaction
1293 between mitochondria and cytoplasmic inclusions is also seen by fluorescence confocal
1294 microscopy in a representative image of a cell co-expressing mito-GFP and NES-RFP-LuciTs.
1295 NES-LuciTs is shown in purple, mitochondria in cyan, and Hoechst counterstain in blue. Scale bar
1296 is 1μm. (e) Representative confocal fluorescence microscopy images taken of WT, fission mutants
1297 (*dnm1Δ* and *fis1Δ*) and fusion mutant (*fzo1Δ* and *ugo1Δ*) cells expressing mito-GFP and NES-
1298 DsRed-LuciTs after 120 minutes at 37 °C and treated with 100μM MG132. Mito-GFP is shown
1299 in cyan, NES-LuciTs in purple, and Hoechst counterstain in blue. Scale bars are 1μm.

1300

1301 **Figure ED5: NVJ -mediated clearance of misfolded proteins.**

1302 (a) Endogenously tagged Nvj1-GFP yeast expressing Ubc9Ts-ChFP were shifted to 37 °C and
1303 monitored by live cell time-lapse fluorescence microscopy for the times shown. White arrowheads
1304 indicate locations of Nvj1 puncta while yellow arrowheads indicate Ubc9Ts-ChFP puncta. Scale
1305 bar is 1μm. (b) WT (top) and *nvj1*Δ (bottom) cells co-expressing NLS-LuciTs and NES-LuciTs
1306 were treated with 100μM MG132 and shifted to 37 °C for 30 mins to preform inclusions. Cells
1307 were then placed in media containing 50mg/ml cycloheximide (CHX) and 100μM MG132 at 37
1308 °C and monitored by live cell time-lapse fluorescence microscopy for the times shown. Scale bars
1309 are 1μm. (c,d) Quantitation of the percentage of cells containing cytoplasmic inclusions in WT,
1310 *nvj1Δ*, and *vac8Δ* yeast co-expressing NLS-EGFP-LuciTs (c) and NES-DsRed-LuciTs (d) after 2
1311 hr at 37 °C with and without treatment with 100μM MG132. A minimum of 500 cells per condition
1312 from 3 biologically independent experiments were counted and unpaired Student's t-tests were
1313 performed comparing the deletion strains to WT with or without MG132 treatment were compared.
1314 P values were adjusted using two-stage linear step-up procedure of Benjamini, Krieger and
1315 Yekutieli with a Q of 5%. (c) %. Adjusted P value for WT vs *nvj1Δ* no MG132 is 0.0205, WT vs
1316 *nvj1Δ* +MG132 is 0.2357, WT vs *vac8Δ* no MG132 is 0.0406, WT vs *vac8Δ* +MG132 is 0.8974,
1317 and WT no MG132 vs WT +MG132 is 0.0239. (d) Adjusted P value for WT vs *nvj1Δ* no MG132
1318 is 0.013, WT vs *nvj1Δ* +MG132 is 0.013, WT vs *vac8Δ* no MG132 is 0.0008, WT vs *vac8Δ*
1319 +MG132 is 0.0447, and WT no MG132 vs WT +MG132 is 0.0005. (e) Levels of EGFP after 1
1320 hour at 37 °C were measured from Quantitative Western blots (mean ± s.e.m. from three
1321 biologically independent experiments). WT and nvj1Δ yeast were compared using an unpaired
1322 Student's t-test resulting in a P value of 0.0043 for WT vs nvj1Δ NLS-LuciTs and NES-LuciTs P
1323 value is 0.0183. Statistics were performed using Prism.

1324 **Figure ED6: ESCRT involvement in the clearance of misfolded proteins.**

1325 (a) Representative confocal images of WT yeast co-expressing Chm7-EGFP and either NLS-
1326 EGFP-LuciTs (left) or NES-DsRed-LuciTs (right) after 120 minutes at 37 °C and treated with
1327 100μM MG132. Chm7 is shown in teal and remains diffuse throughout the cell, NLS-EGFP-
1328 LuciTs in green, NES-DsRed-LuciTs in purple, nuclear pores in gold and Hoechst counterstain in
1329 blue. Scale bar is 1μm. (b) Representative confocal images of WT and *vps23Δ*,
1330 *vps34Δ,* and *vps15Δ* yeast co-expressing NLS-EGFP-LuciTs and NES-DsRed-LuciTs after 2 hr at
1331 37 °C and treated with 100μM MG132. NLS-EGFP-LuciTs is shown in green, NES-DsRed-
1332 LuciTs in purple, nuclear pores in gold, and Hoechst counterstain in blue. Insets show the budding
1333 INQ encapsulated by nuclear pores. Scale bars are 1μm. Same data as shown in Figure 6c, but with
1334 the green channel separated to clearly detail the colocalization with the cytoplasmic protein.

1335 **Figure ED7: Vacuole-mediated clearance of INQ and JUNQ.**

1336 (a) Representative images of WT cells expressing NES-2xKeima-LuciTs after 2 hr incubation at 37
1337 °C with 100μM MG132. Over time, fluorescence is seen with excitation in the 589nm channel
1338 indicating the NLS-LuciTs has encountered an acidic environment. Insets show the transition from
1339 green to red and a structure leaving the inclusion that is fully red. Scale bars are 5 uM. Same data
1340 shown in Figure 7d, but with more time points and a larger field of view in the images. (b) WT cells
1341 expressing NES-2xKeima-LuciTs after 85 min incubation at 37 °C with 100μM MG132. (c) Longer
1342 exposure of the blot shown in Figure 7f to highlight the difference in the number and pattern of the
1343 GFP bands in the WT vs *pep4Δ* cells. (d) Levels of EGFP at time 0 were measured from
1344 Quantitative Western blots such as those shown in Figure 7e, f (mean ± s.e.m. from three
1345 biologically independent experiments). WT and *pep4Δ* yeast were compared using an unpaired
1346 Student's t-test without reaching statistical significance. (e) WT yeast expressing NLS-GFP-LuciTs

1347 were treated with 8uM of FM4-64 and incubated for 2hr at 37 °C with 100μM MG132. Cells were
1348 imaged every 30 sec for 90 mins. Scale bar is 1μm. Same data shown in Figure 7h, but only WT
1349 and with more timepoints during the entry into the vacuole.

1350

1351 **Legends to movies**

1352 Movie 1. Live-cell time-lapse fluorescence microscopy of WT cells expressing NLS-LuciTs (left)
1353 or NES-LuciTs (right) at 37 °C, treated with 100μM MG132. Same data shown in stills in Figure
1354 1c (left), d (right).

1355 Movie 2. Dynamic representation of the 3D reconstructions of the data shown in Figure 1e (left),g
1356 (right). Videos were created in Volocity.

1357 Movie 3. Dynamic representation of the 3D reconstructions of the data shown in Figure 2a (left),
1358 b (right). Videos were created in Volocity.

1359 Movie 4. Live-cell time-lapse fluorescence microscopy of the data shown in Figure 3a.

1360 Movie 5. Dynamic representation of the data shown in Figure 3b.

1361 Movie 6. Dynamic representation of the 3D reconstruction of the data shown in Figure 3c. Video
1362 was created in Volocity.

1363 Movie 7. Dynamic representation of the 3D reconstruction shown in Figure 4c. Video was created
1364 in Amira.

1365 Movie 8. Dynamic representation of the 3D reconstruction shown in Figure 4d,f. Video was
1366 created in Amira.

1367 Movie 9. Live-cell time-lapse fluorescence microscopy of the data shown in Figure 5a.

1368 Movie 10. Dynamic representation of the 3D reconstruction of the data shown in Figure 5c. Video
1369 was created in Volocity.

1370 Movie 11. Dynamic representation of the 3D reconstruction of the data shown in Figure 5b. Video
1371 was created in Volocity.

1372 Movie 12. Live-cell time-lapse fluorescence microscopy of the data shown in Figure 5f shown at
1373 5 frames per second.

1374 Movie 12b. Live-cell time-lapse fluorescence microscopy of the data shown in Figure 5f shown at
1375 2 frames per second.

1376 Movie 12c. Live-cell time-lapse fluorescence microscopy of the data shown in Figure 5f shown at
1377 2 frames per second. Only the 488nm channel is shown in greyscale.

1378 Movie 13. Dynamic representation of the 3D reconstruction of the data shown in Figure 5e. Video
1379 was created in Volocity.

1380 Movie 14. Live-cell time-lapse fluorescence microscopy of the WT cell data shown in Figure 5h.

1381 Movie 15. Live-cell time-lapse fluorescence microscopy of the *nvj1Δ* cell data shown in Figure
1382 5h.

1383 Movie 16. Live-cell time-lapse fluorescence microscopy of the *vps4Δ* cell data shown in Figure
1384 5h.

Sontag et al.
Figure 1

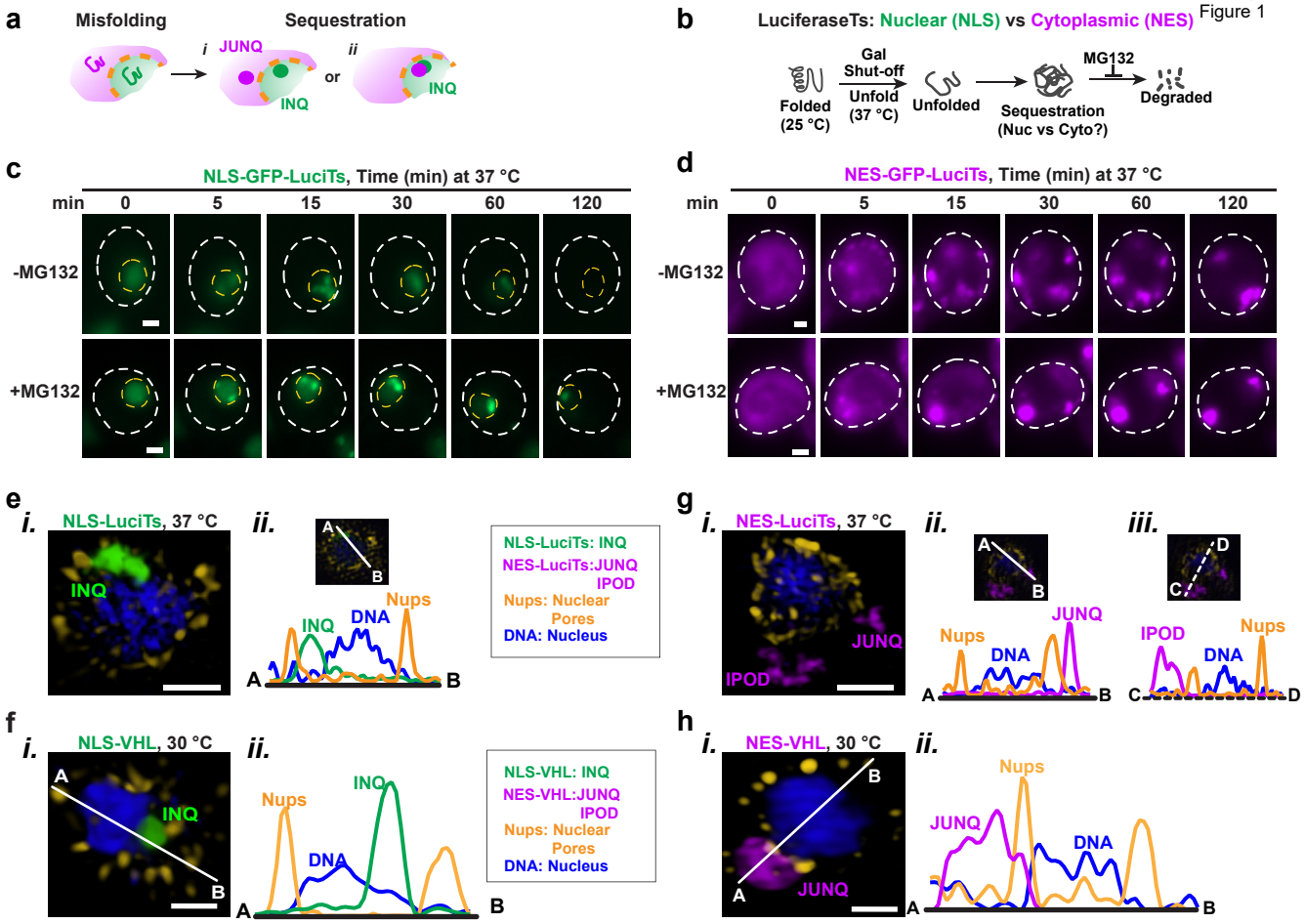

Sontag et al.
Figure 2

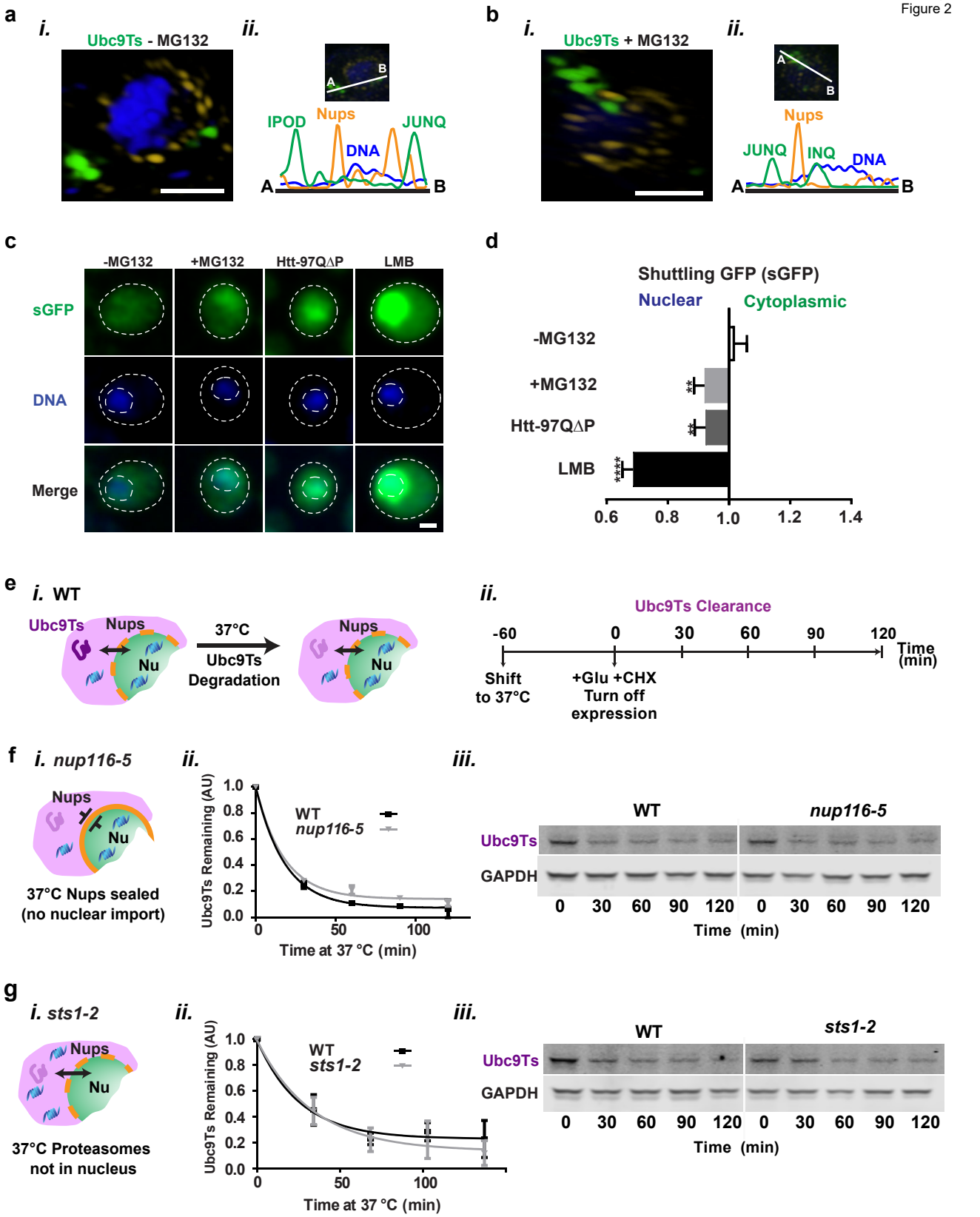

Sontag et al.
Figure 3

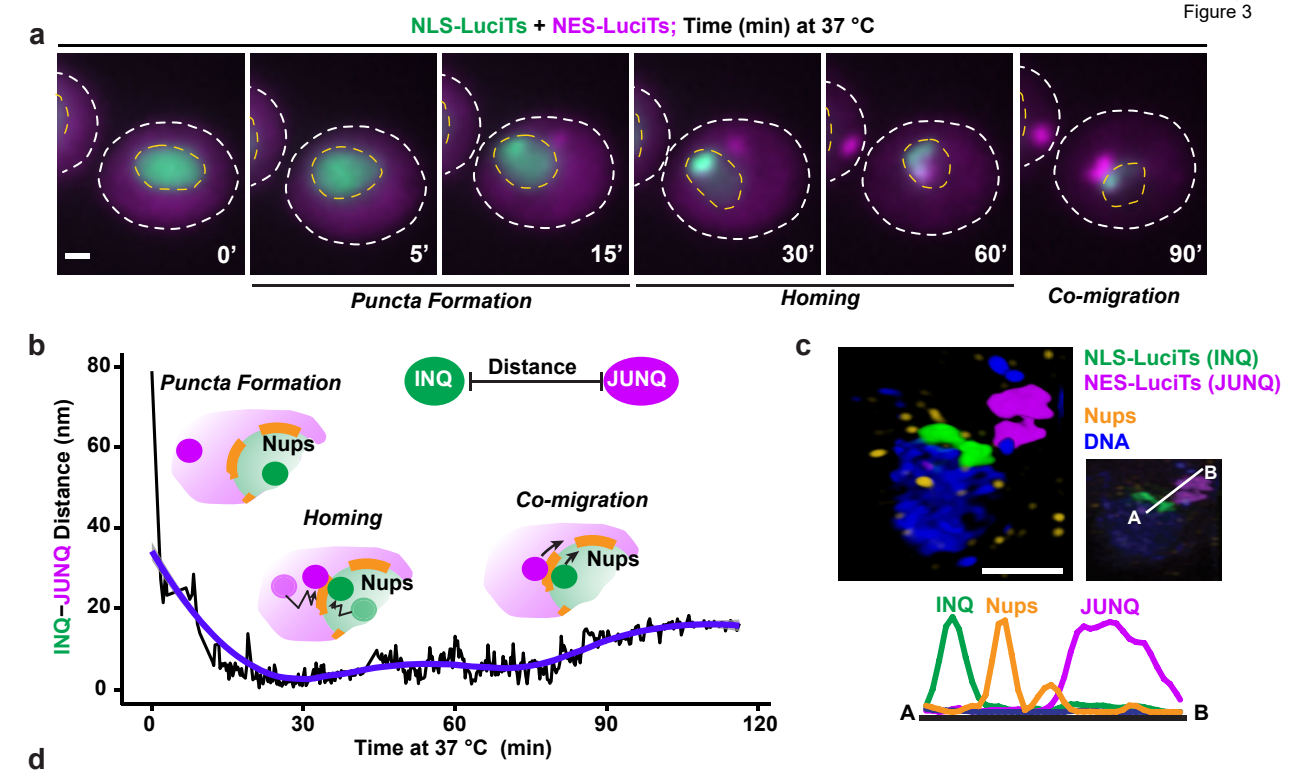

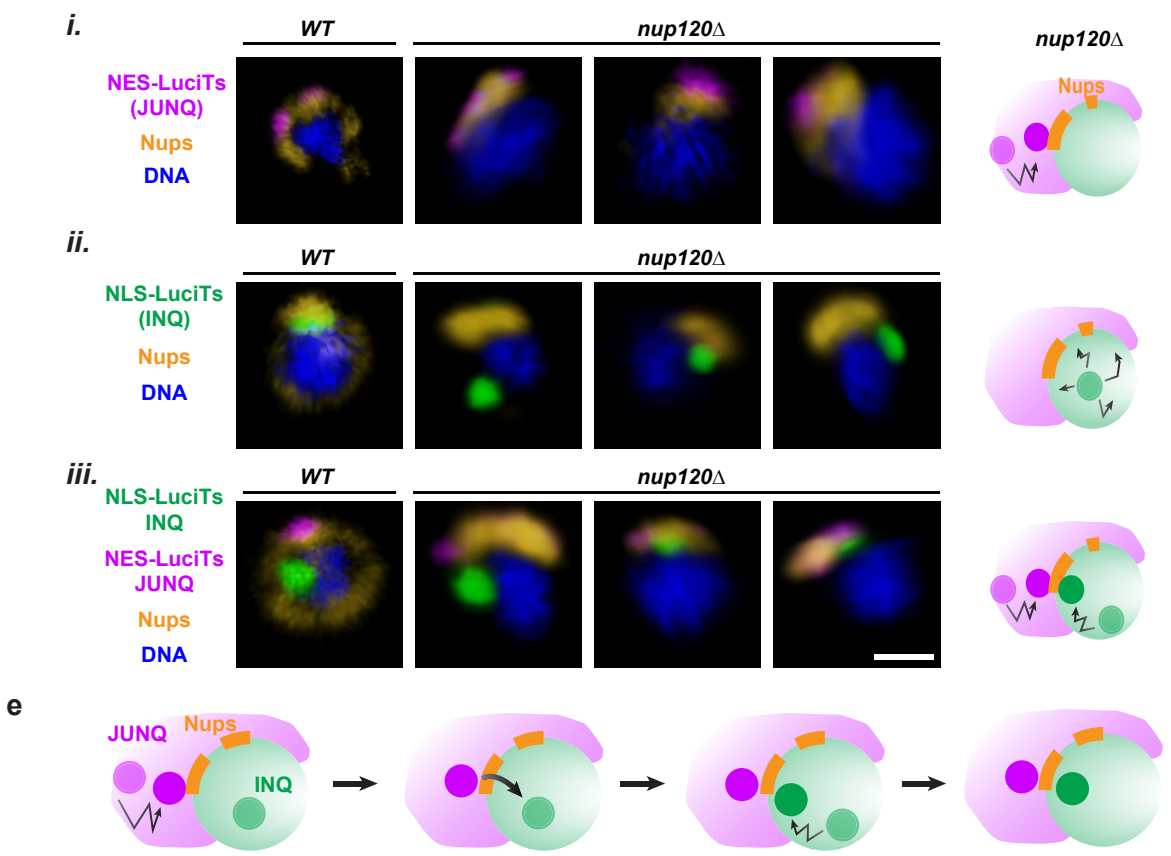

Sontag et al.
Figure 4

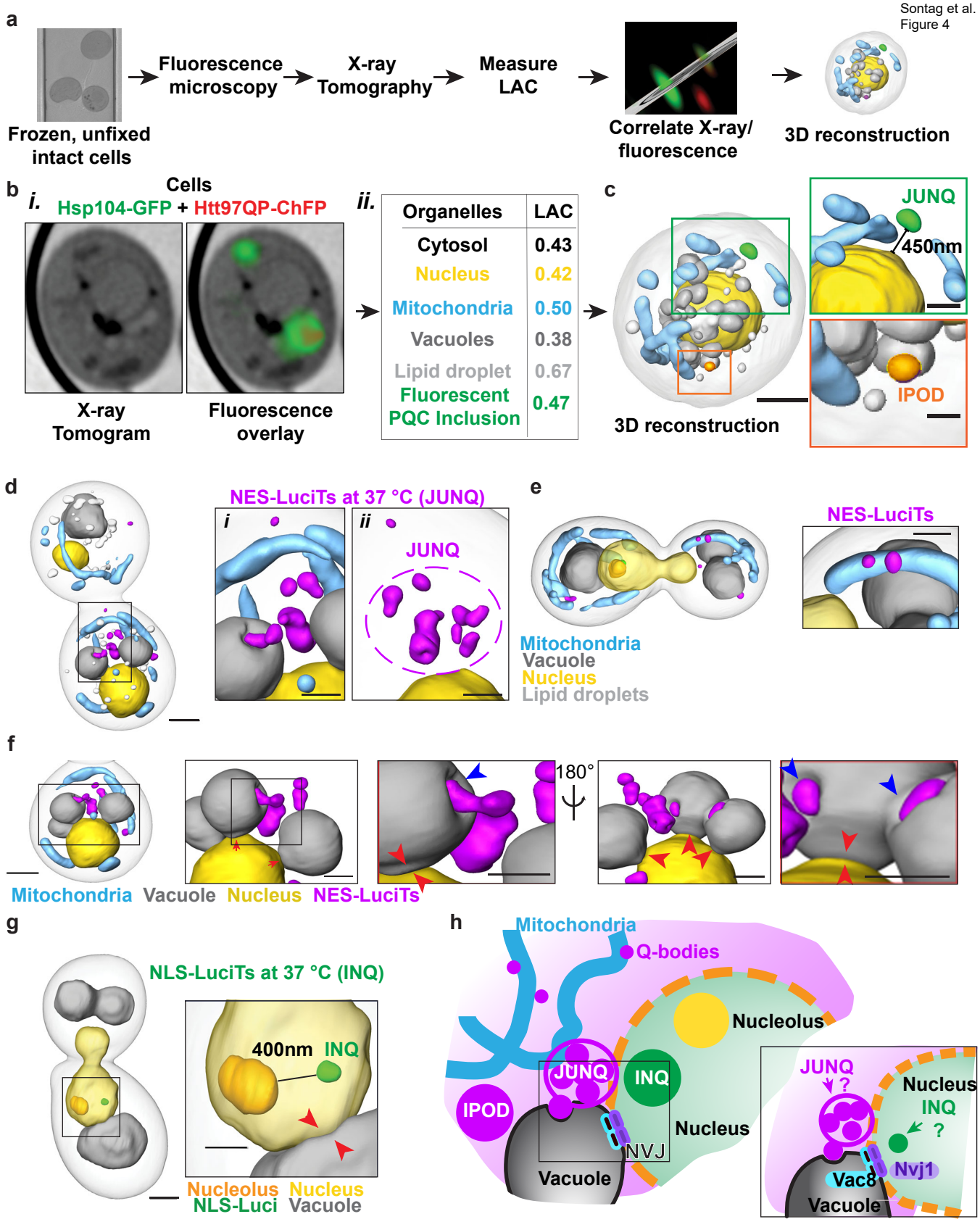

Sontag et al.
Figure 5

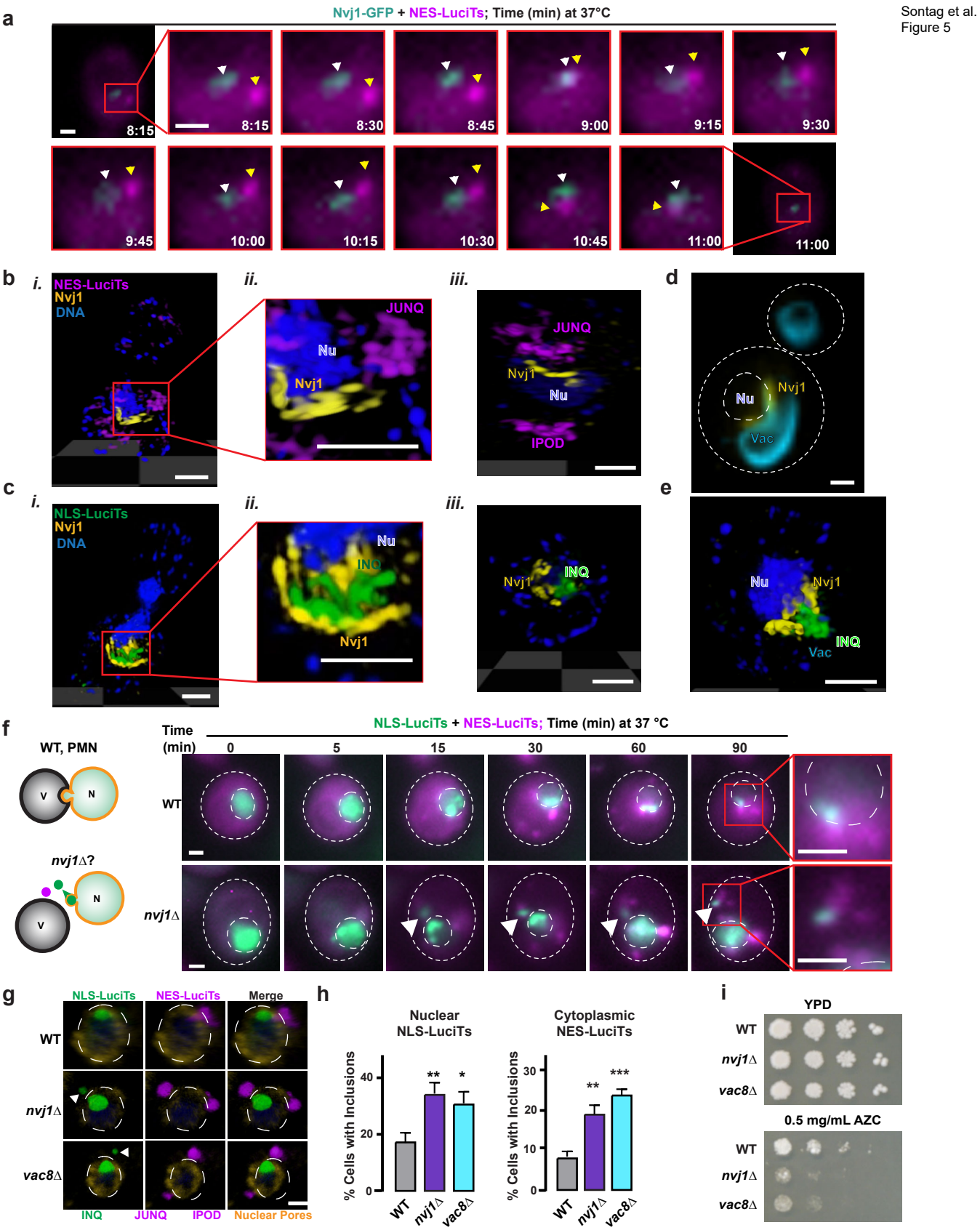

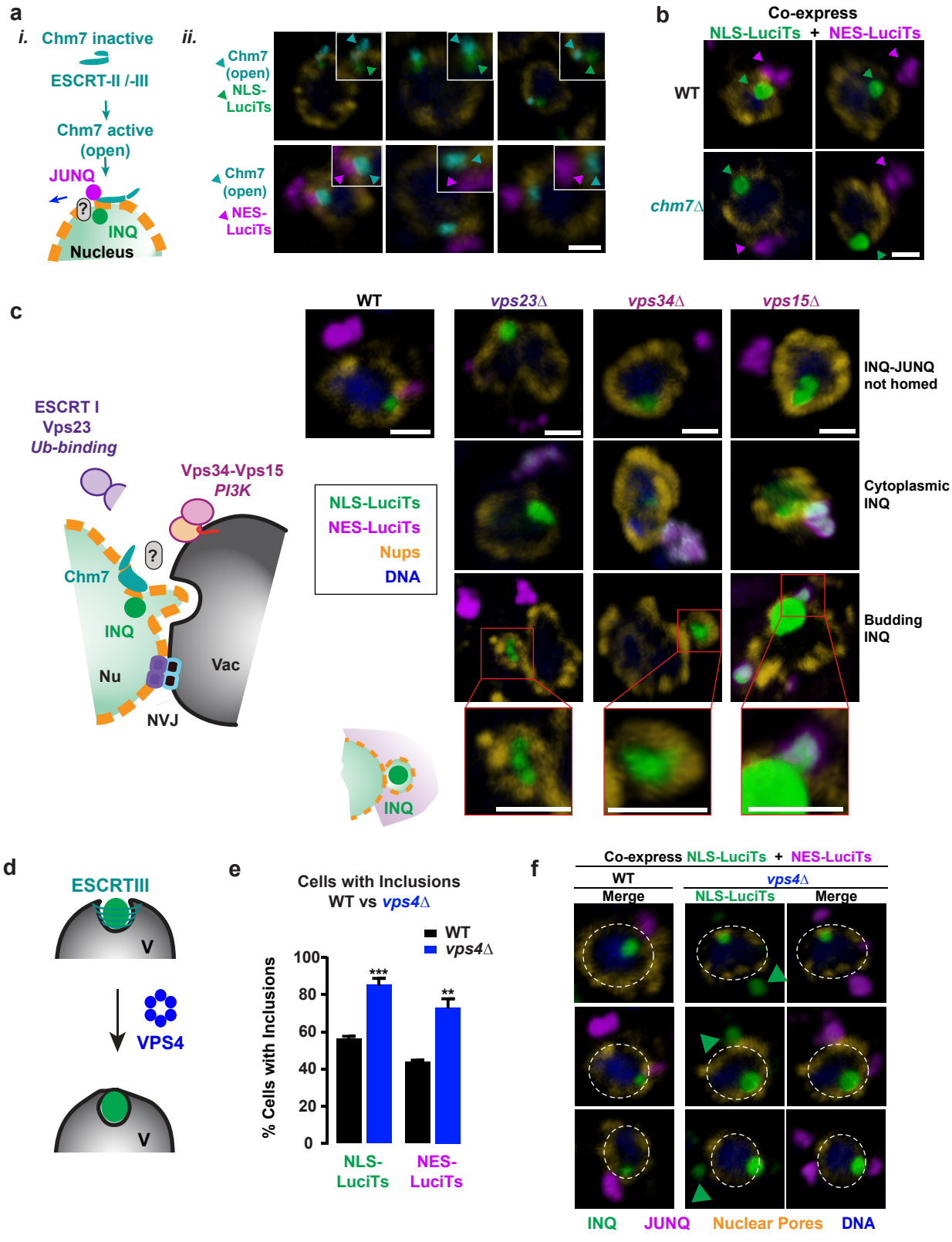
a
i.
Chm7 inactive
ESCRT-II /-III
Chm7 active
(open)
JUNQ
?
INQ
Nucleus
ii.
Chm7
(open)
NLS-
LuciTs
Chm7
(open)
NES-
LuciTs
b
Co-express
NLS-LuciTs + NES-LuciTs
WT
chm7Δ
c
ESCRT I
Vps23
Ub-binding
Vps34-Vps15
PI3K
Chm7
?
INQ
Nu
Vac
NVJ
WT
vps23Δ
vps34Δ
vps15Δ
INQ-JUNQ
not homed
Cytoplasmic
INQ
Budding
INQ
NLS-LuciTs
NES-LuciTs
Nups
DNA
INQ
d
ESCRTIII
V
VPS4
V
e
Cells with Inclusions
WT vs vps4Δ
WT
vps4Δ
% Cells with Inclusions
100
80
60
40
20
0
***
**
NLS-
LuciTs
NES-
LuciTs
f
Co-express NLS-LuciTs + NES-LuciTs
WT
vps4Δ
Merge
NLS-LuciTs
Merge
INQ
JUNQ
Nuclear Pores
DNA

Sontag et al.
Figure 7

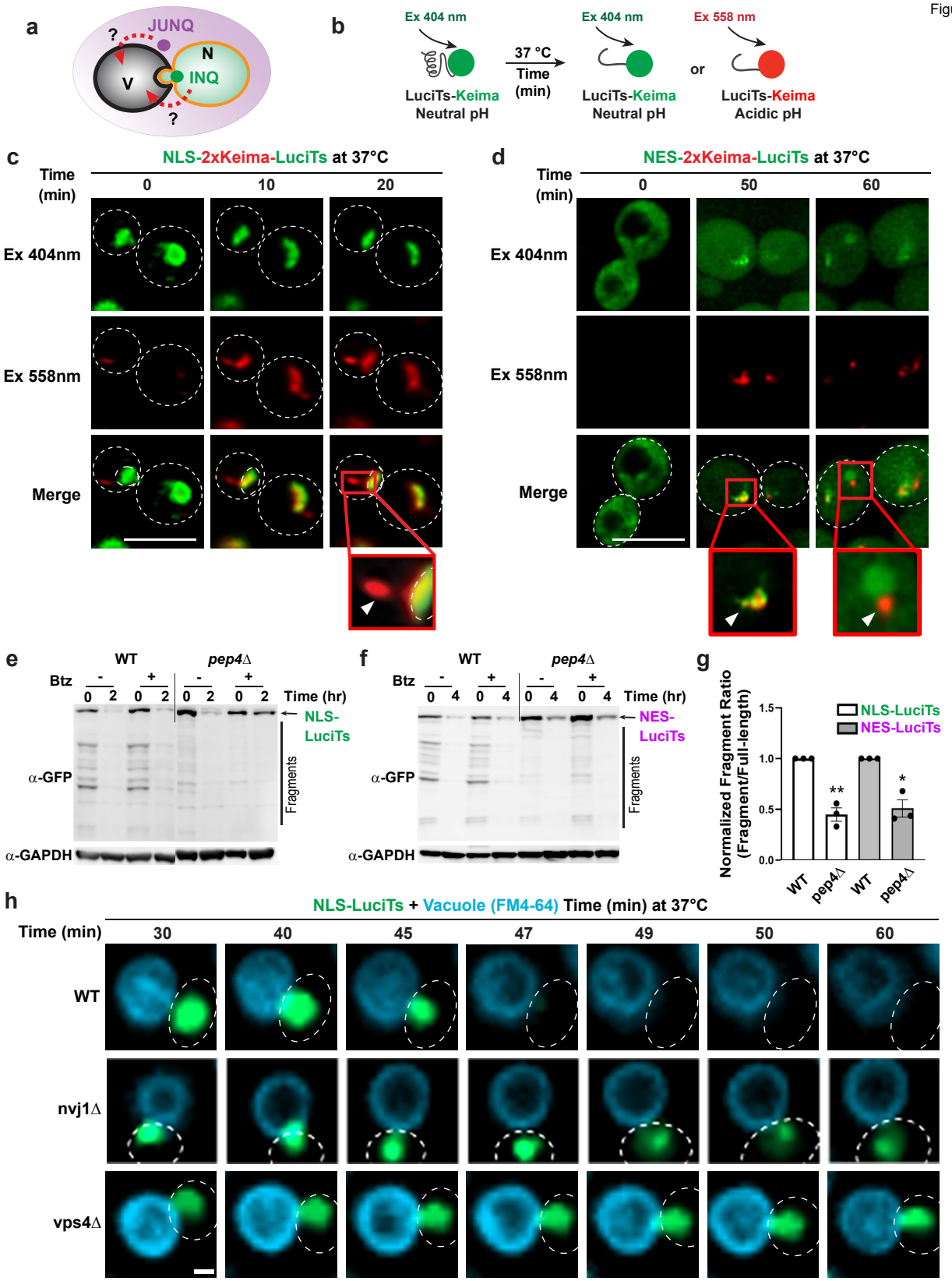

Sontag et al.
Figure 8

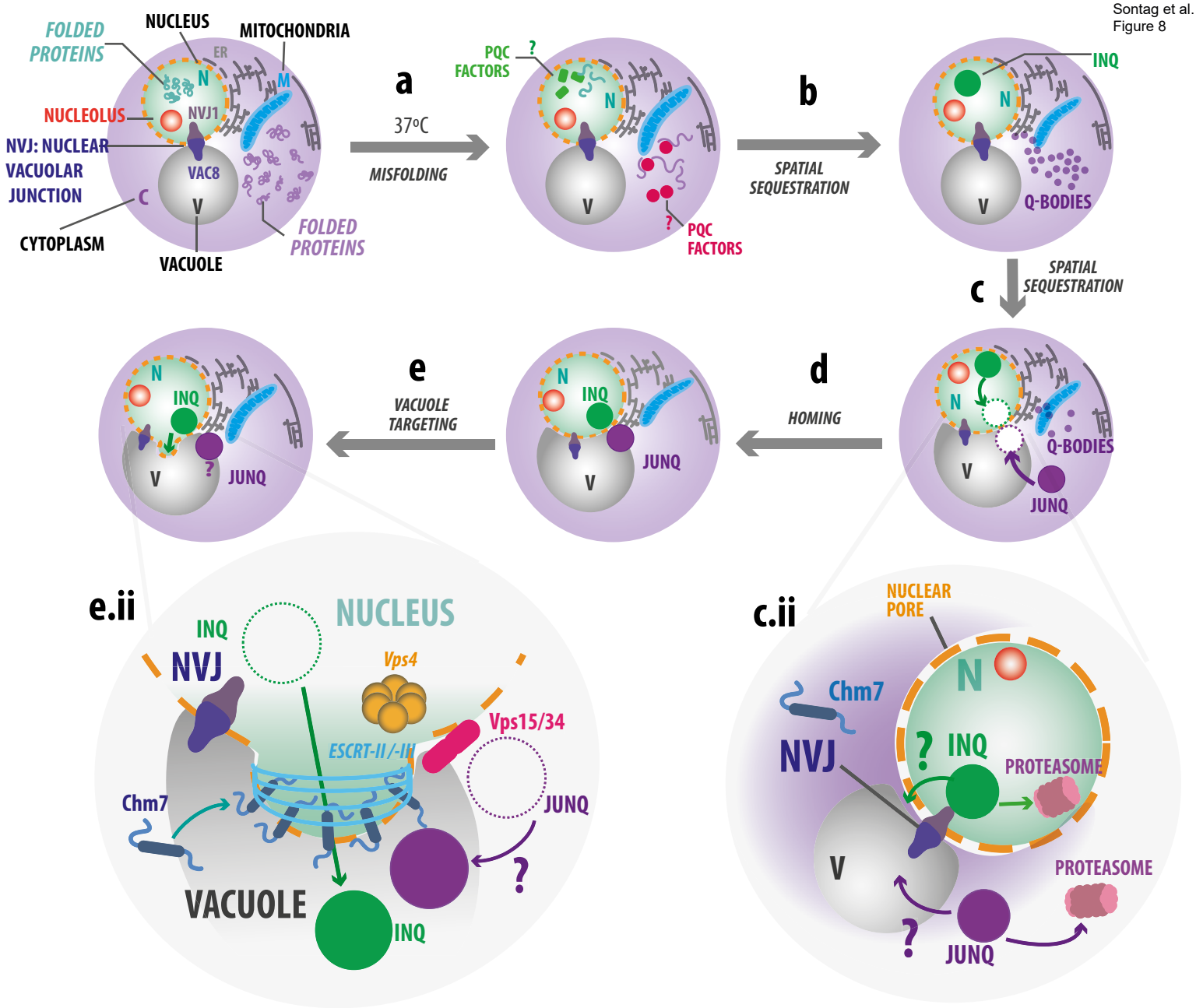

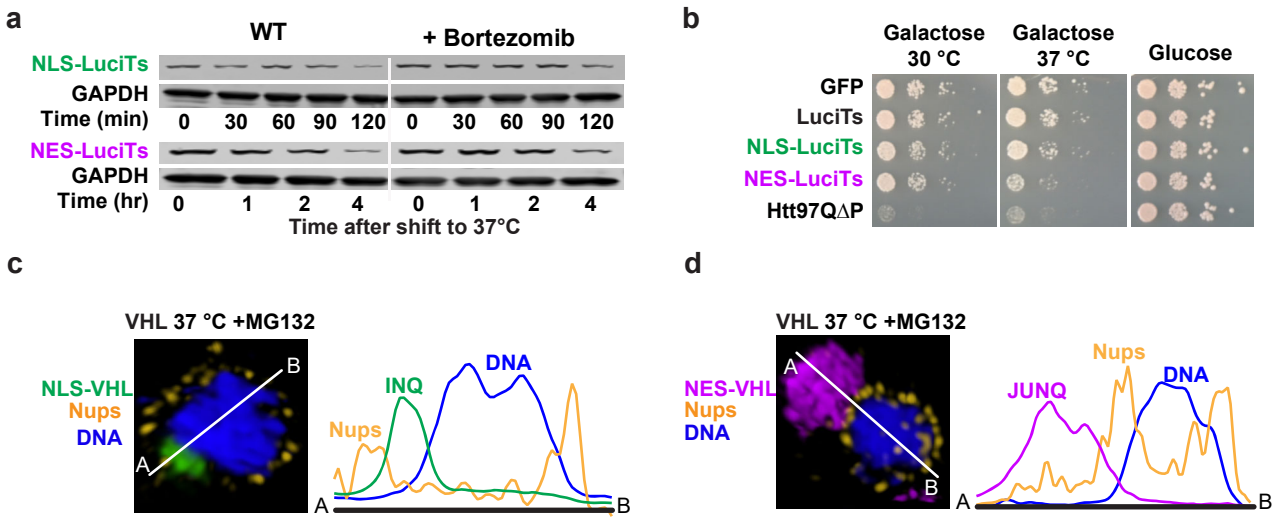
a
WT
+ Bortezomib
NLS-LuciTs
GAPDH
Time (min)
0 30 60 90 120 0 30 60 90 120
NES-LuciTs
GAPDH
Time (hr)
0 1 2 4 0 1 2 4
Time after shift to 37°C
b
Galactose 30 °C
Galactose 37 °C
Glucose
GFP
LuciTs
NLS-LuciTs
NES-LuciTs
Htt97QΔP
c
VHL 37 °C +MG132
NLS-VHL
Nups
DNA
A
B
INQ
DNA
Nups
d
VHL 37 °C +MG132
NES-VHL
Nups
DNA
JUNQ
Nups
DNA

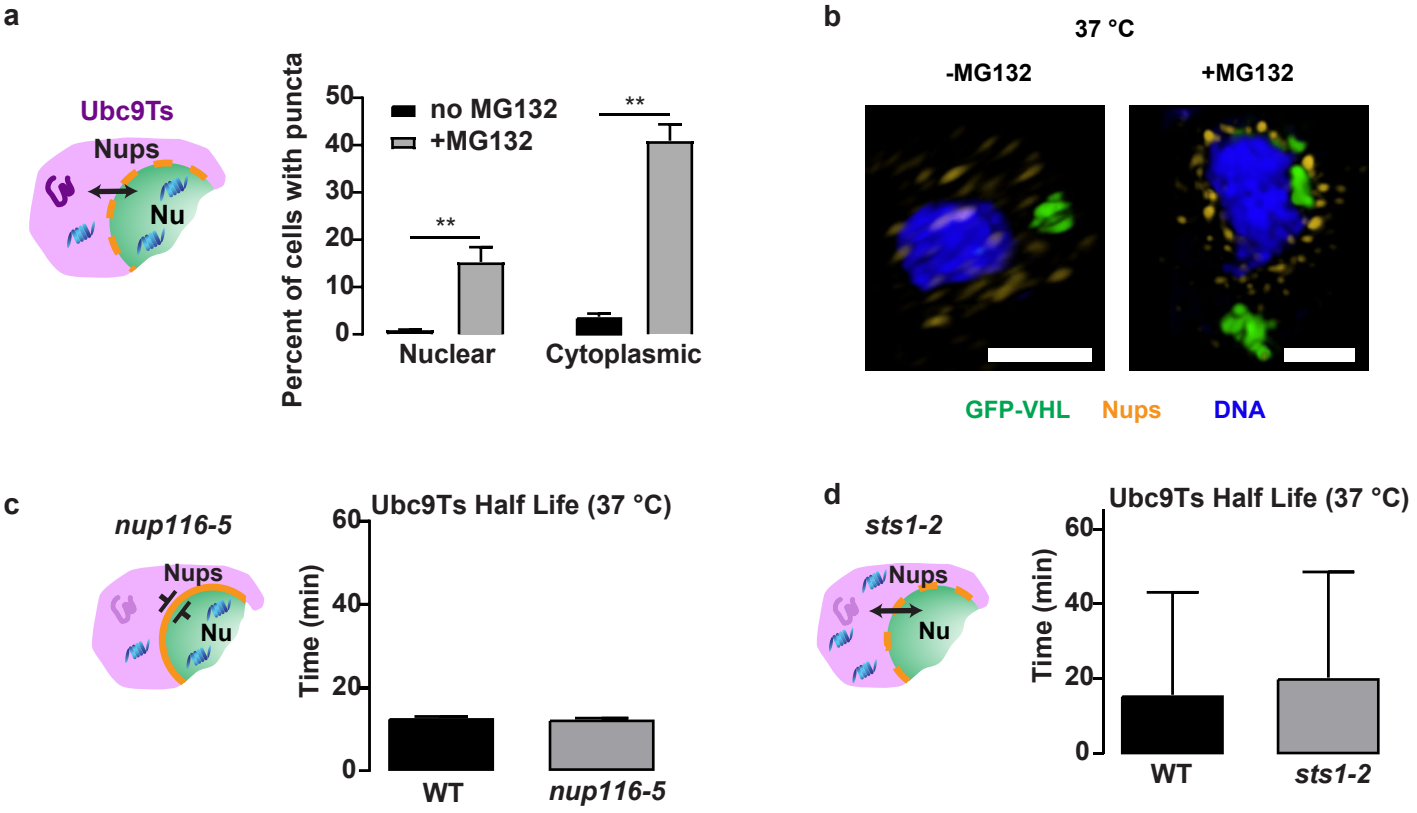
a
Ubc9Ts
Nups
Nu
Percent of cells with puncta
50
40
30
20
10
0
no MG132
+MG132
**
**
Nuclear
Cytoplasmic
b
37 °C
-MG132
+MG132
GFP-VHL
Nups
DNA
c
nup116-5
Nups
Nu
Ubc9Ts Half Life (37 °C)
Time (min)
60
40
20
0
WT
nup116-5
d
sts1-2
Nups
Nu
Ubc9Ts Half Life (37 °C)
Time (min)
60
40
20
0
WT
sts1-2

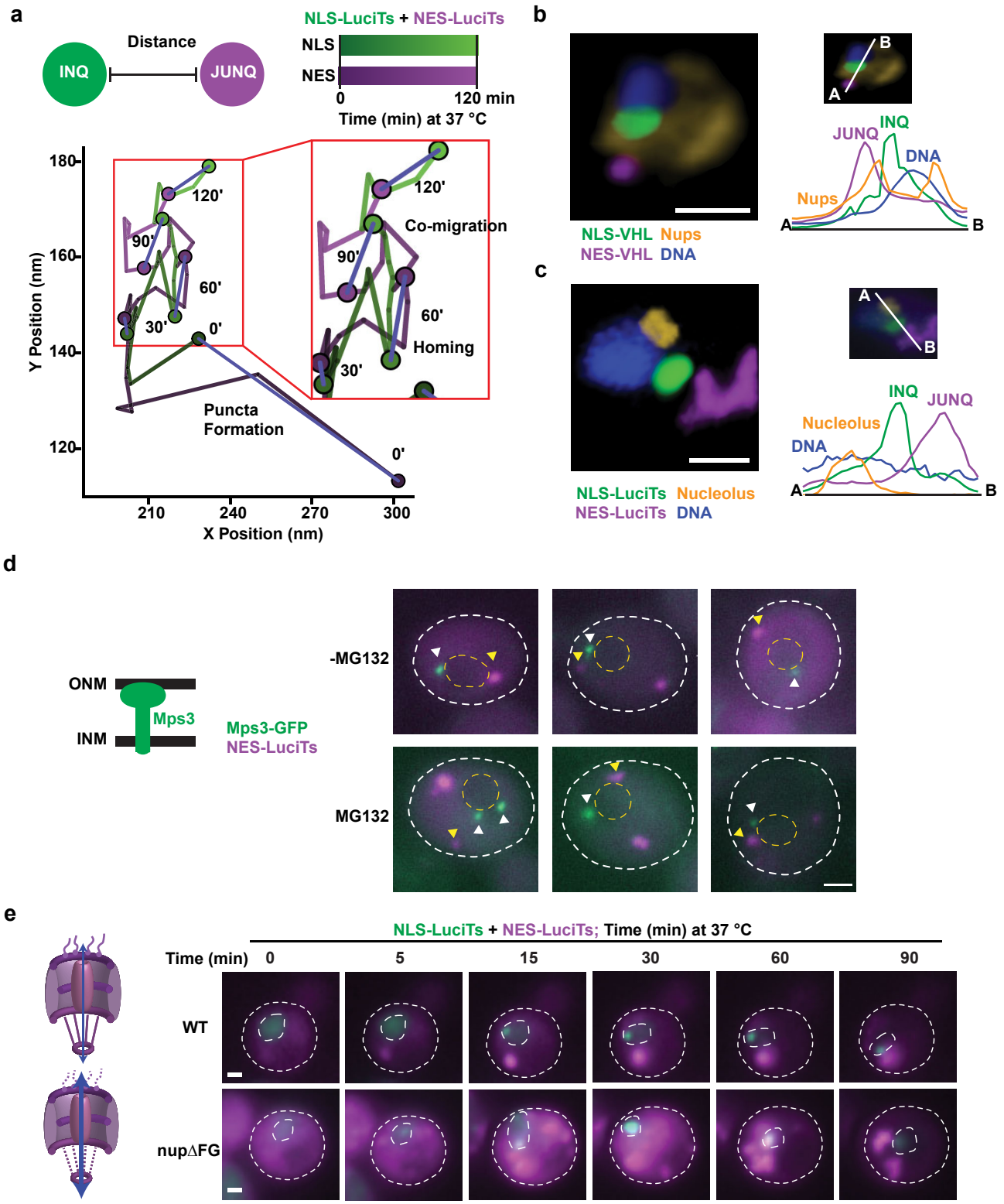
a
INQ
Distance
JUNQ
NLS-LuciTs + NES-LuciTs
NLS
NES
0
120 min
Time (min) at 37 °C
Y Position (nm)
X Position (nm)
180
160
140
120
210
240
270
300
120'
90'
60'
30'
0'
Co-migration
Homing
Puncta
Formation
b
NLS-VHL Nups
NES-VHL DNA
A
B
JUNQ
INQ
DNA
Nups
c
NLS-LuciTs Nucleolus
NES-LuciTs DNA
Nucleolus
d
ONM
INM
Mps3
Mps3-GFP
NES-LuciTs
-MG132
MG132
e
NLS-LuciTs + NES-LuciTs; Time (min) at 37 °C
Time (min)
0
5
15
30
60
90
WT
nupΔFG

Sontag et al.
Figure ED4

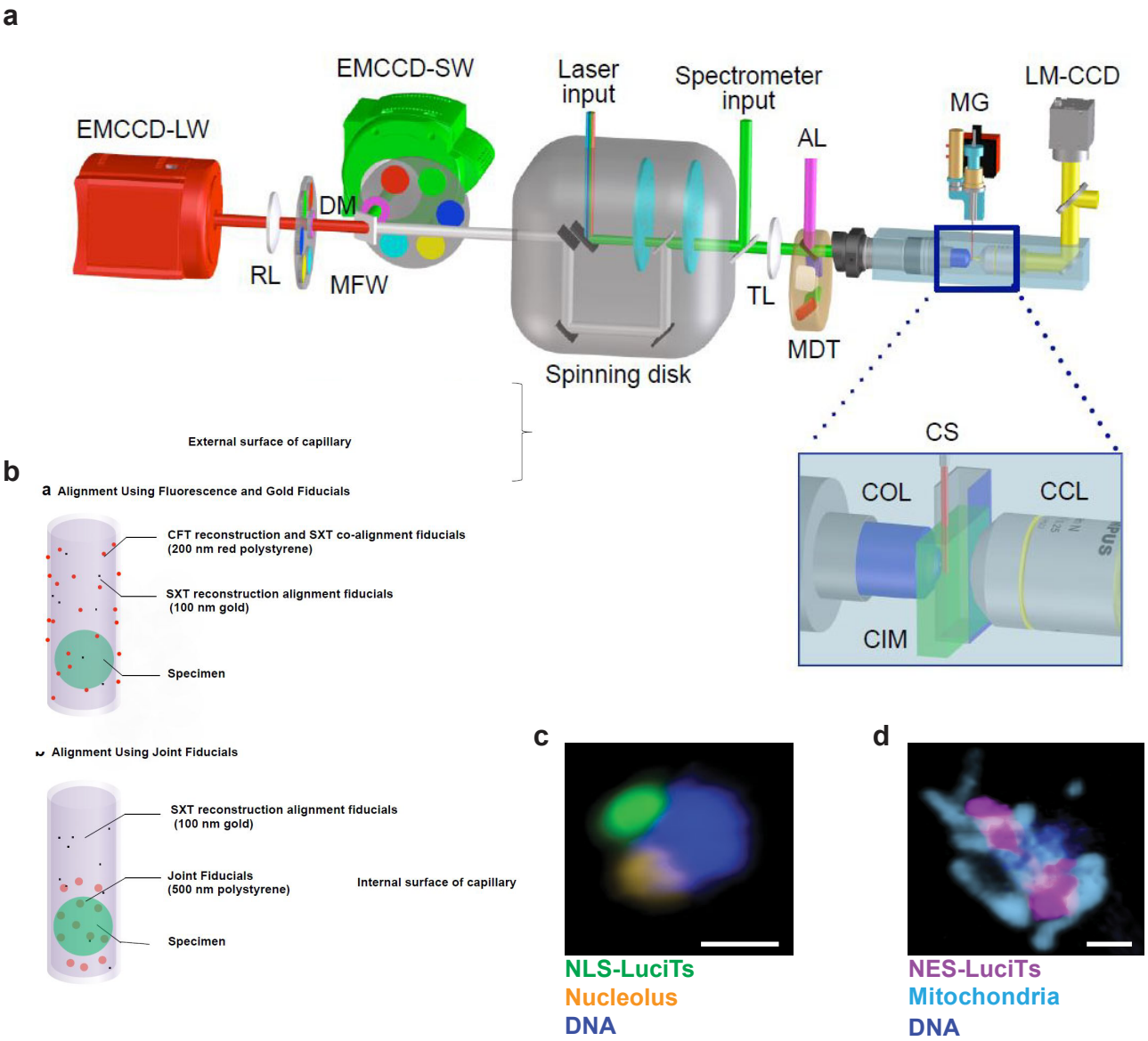

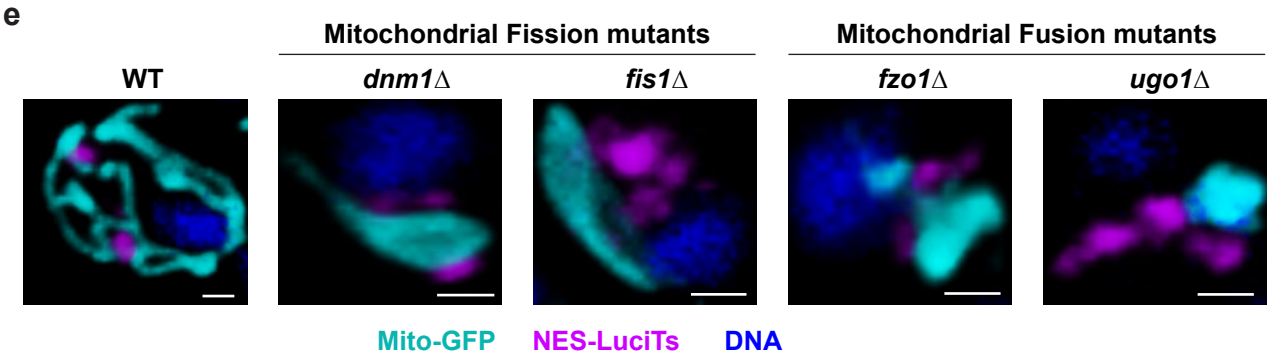

Sontag et al.
Figure ED5

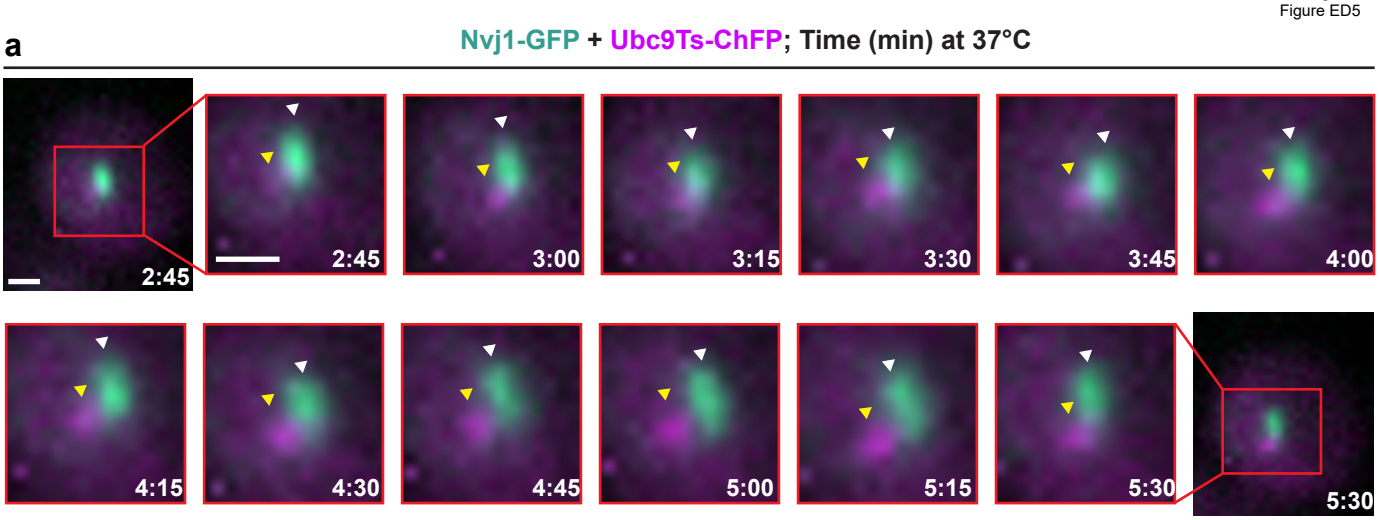

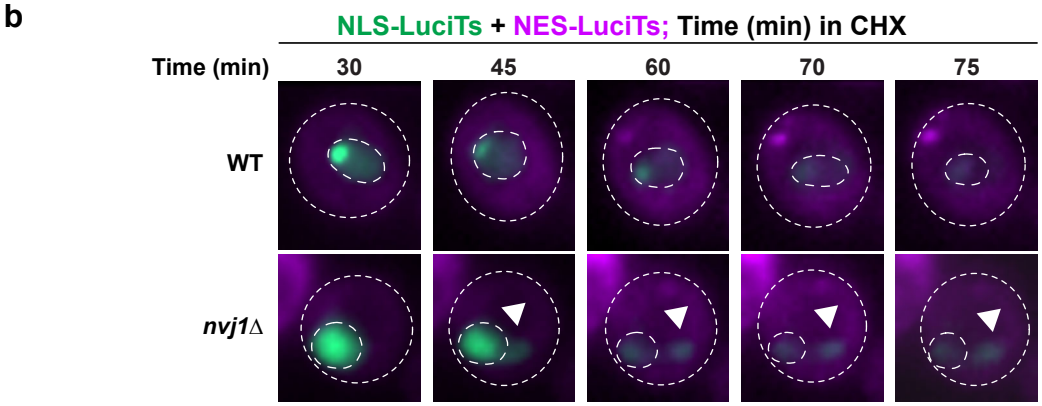

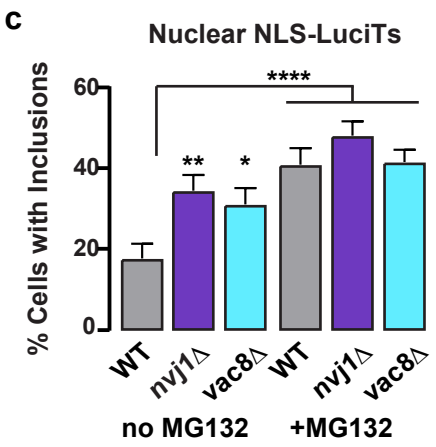

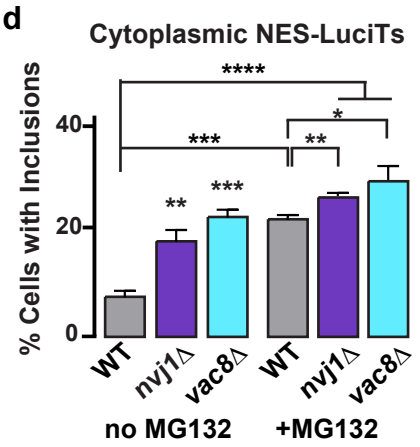

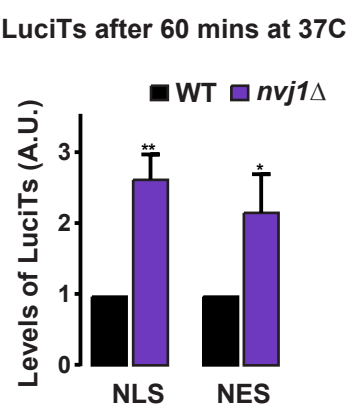

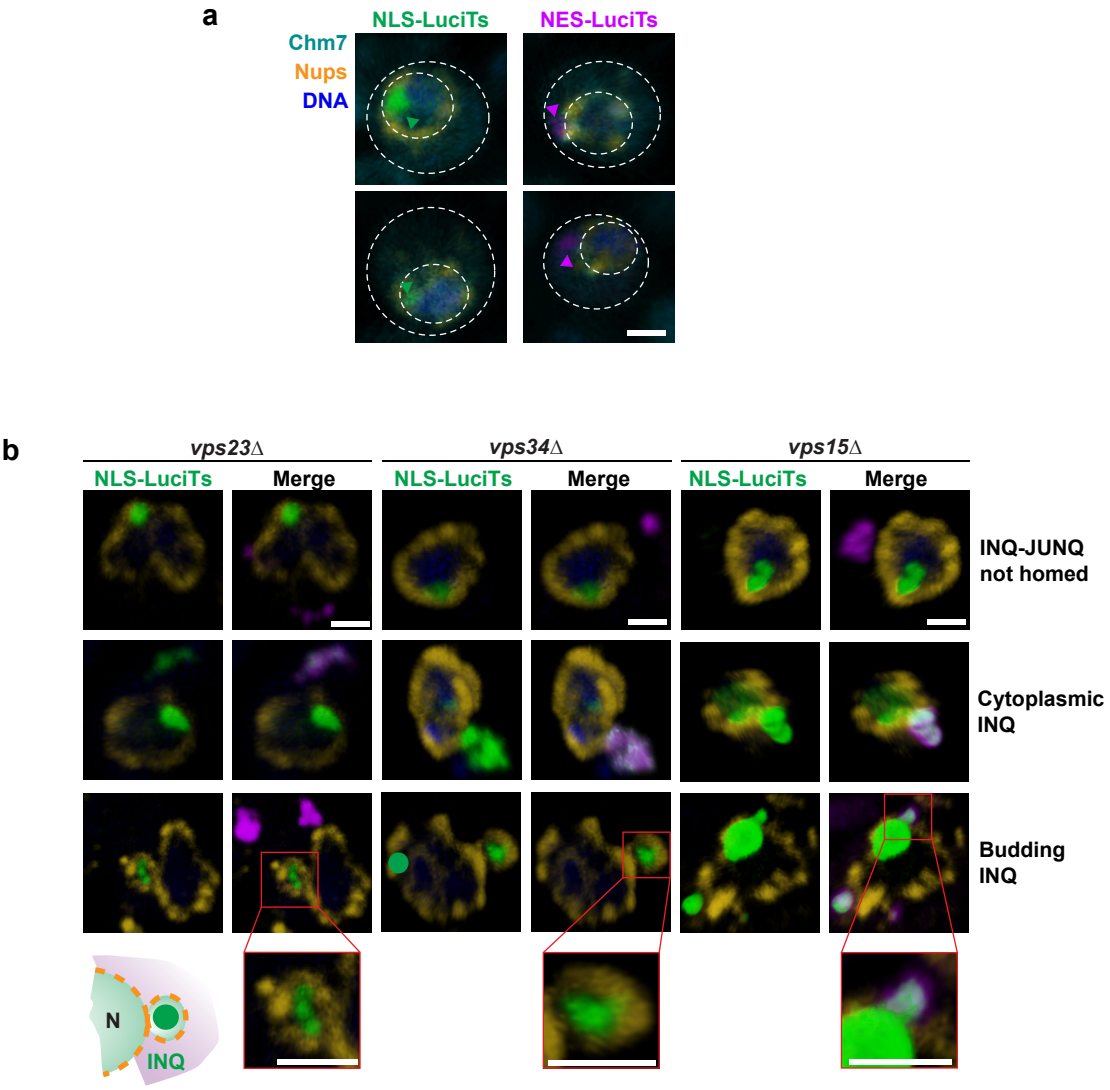
a
NLS-LuciTs
NES-LuciTs
Chm7
Nups
DNA
b
vps23Δ
vps34Δ
vps15Δ
NLS-LuciTs
Merge
NLS-LuciTs
Merge
NLS-LuciTs
Merge
INQ-JUNQ
not homed
Cytoplasmic
INQ
Budding
INQ
N
INQ

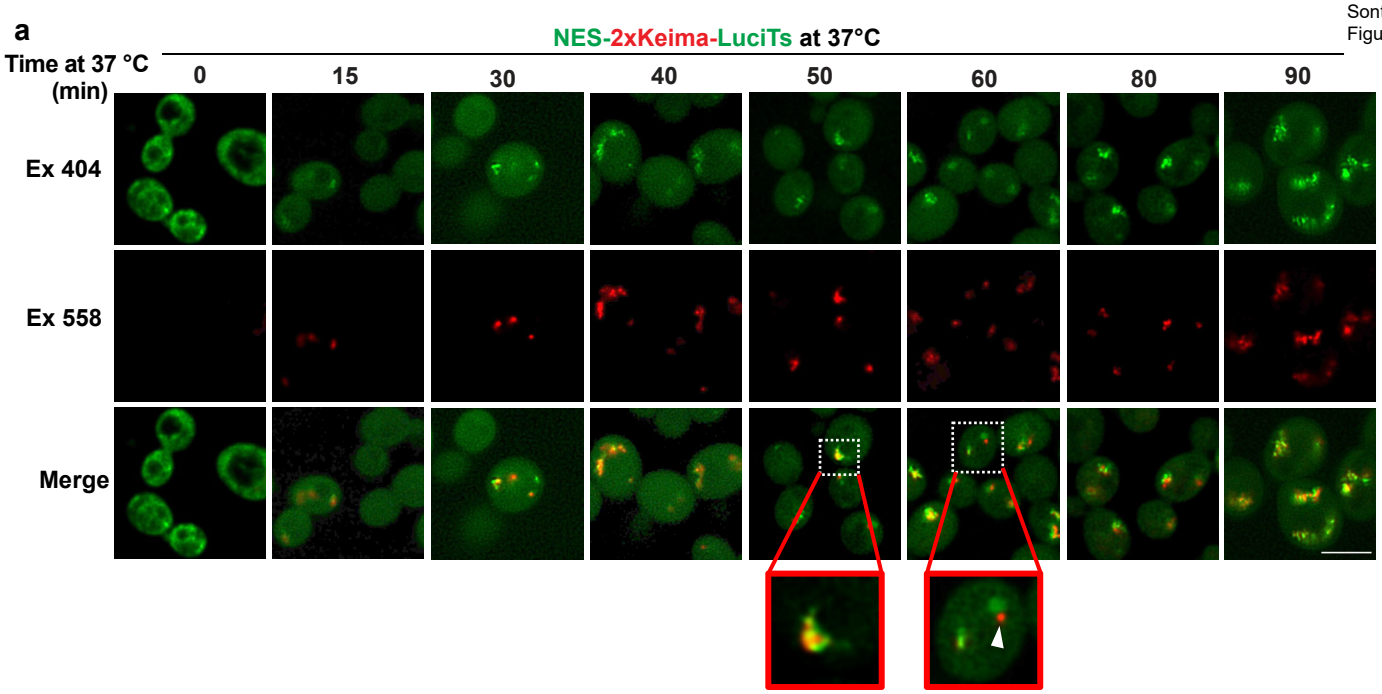
a
NES-2xKeima-LuciTs at 37°C
Time at 37 °C (min)
0
15
30
40
50
60
80
90
Ex 404
Ex 558
Merge

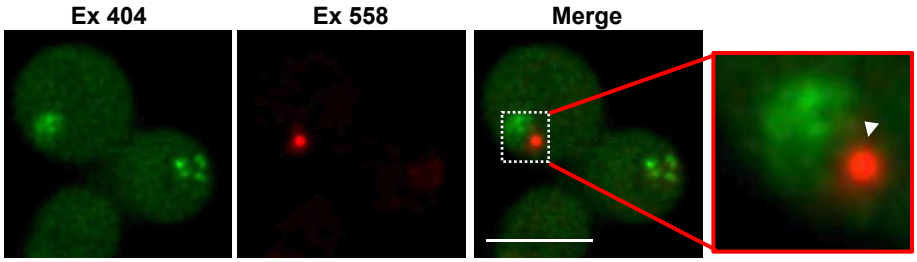
b
NES-2xKeima-LuciTs 85 min chase at 37°C
Ex 404
Ex 558
Merge

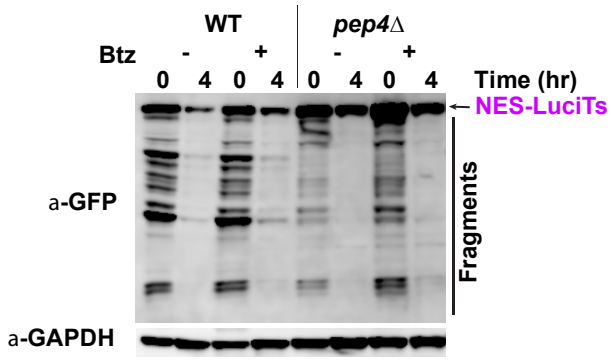
c
WT
pep4Δ
Btz
-
+
-
+
0
4
0
4
0
4
0
4
Time (hr)
NES-LuciTs
Fragments
a-GFP
a-GAPDH

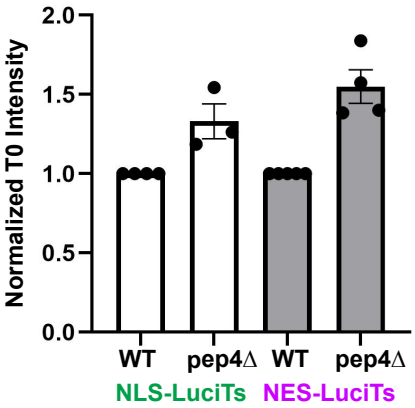
d
Normalized T0 Intensity
2.0
1.5
1.0
0.5
0.0
WT
pep4Δ
WT
pep4Δ
NLS-LuciTs
NES-LuciTs

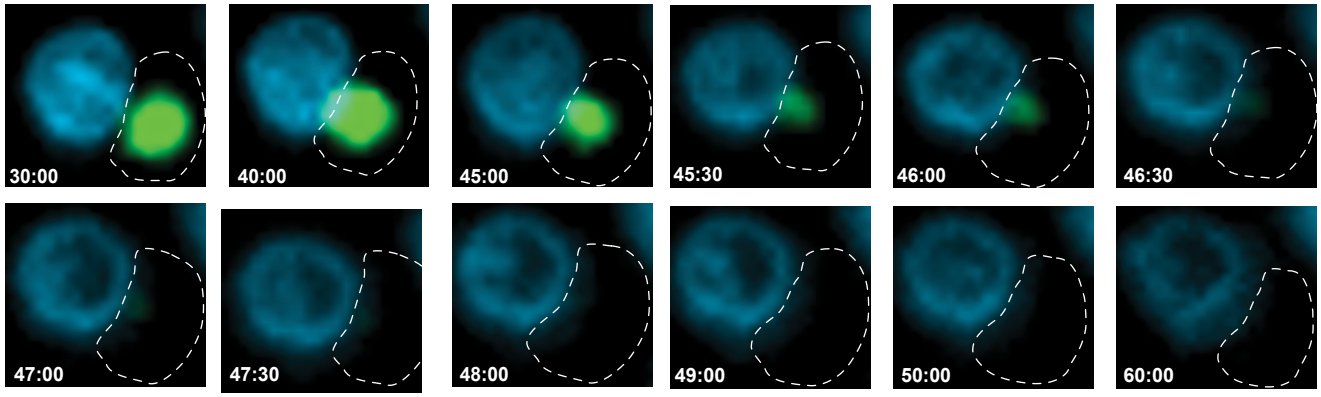
e
WT Chase Time at 37 °C (min)
NLS-LuciTs
Vacuole
30:00
40:00
45:00
45:30
46:00
46:30
47:00
47:30
48:00
49:00
50:00
60:00

SUPPLEMENTARY TABLE S1. Genotypes and sources of yeast strains used in this study				
Nr.	**NAME**	**GENOTYPE**	**SOURCE AND COMMENTS**	
ESY 1	BY4741			
ESY 104	W303			
ESY 105	CRM1		WT strain for crm1-T539C	from Michael Rosbash
ESY 106	crm1-T539C		has nuclear export deficiency with leptomycin B treatment	from Michael Rosbash
ESY 95	Nup116-5	nup116-5::HIS3	SWY027	from Susan Wente
ESY 96	STS1		WT strain for sts1-2	from Kiran Madura
ESY 97	sts1-2		temperature sensitive mutation that blocks proteasome import into the nucleus	from Kiran Madura
ESY 113	*dnm1*	BY4741 Mata	Deletion collection	
ESY 119	*fis1*	BY4741 Mata	Deletion collection	
ESY 122	*fzo1*	BY4741 Mata	Deletion collection	
ESY 123	*ugo1*	BY4741 Mata	Deletion collection	
ESY 121	Mps3-GFP	BY4741 Mata	GFP collection	
ESY 127	*nup120*	BY4741 Mata	Deletion collection	
ESY 94	*nup⊿FG*		SWY3042	from Susan Wente
ESY 14	Nvj1-GFP	BY4741 Mata	GFP collection	
ESY 4	*nvj1*	BY4741 Mata	Deletion collection	
ESY 3	*vac8*	BY4741 Mata	Deletion collection	
ESY 150	*vps4*	BY4741 Mata	Deletion collection	
ESY177	Chm7OPEN-GFP	W303, chm7OPEN-(1-369)-GFP::HIS3	DTCPL413	From Patrick Lusk
ESY183	*Chm7*	W303, chm7Δ::hphMX6		From Patrick Lusk
ESY182	Chm7-GFP	W303, CHM7-GFP::HIS3		From Patrick Lusk
FMP1X	Nvj1-sfGFP	BY4741 Mata	NVJ1 GFP C-terminally tagged	This study

SUPPLEMENTARY TABLE S2. Plasmids used in this study		
Nr.	**NAME**	**SOURCE AND COMMENTS**
ES p331	NLS-GFP-LuciTs	This study
ES p357	NES-DsRed-LuciTs	This study
ES p325	NLS-GFP-VHL	This study and (Samant et al. 2018)
ES p355	NES-DsRed-VHL	This study and (Samant et al. 2018)
ES p20	Ubc9Ts-GFP	(Escusa-Toret et al. 2013)
ES p562	Ubc9Ts-ChFP	(Escusa-Toret et al. 2013)
ES p144	GFP-VHL	(Escusa-Toret et al. 2013)
ES p536	pRS NLS-GFP2-NES	(Stade et al., 1997)
ES p57	mHTT 97QP-ChFP	(Escusa-Toret et al. 2013)
ES p520	vt100 GFP	(Westermann et al. 2000)
FMP 1X	NLS-Keima-LuciTs	This study
FMP 1Y	NLS-2xKeima-LuciTs	This study
FMP 2X	NES-Keima-LuciTs	This study
FMP 2Y	NES-2xKeima-LuciTs	This study